GSK3 inhibition rescues growth and telomere dysfunction in dyskeratosis congenita iPSC-derived type II alveolar epithelial cells

Rafael J Fernandez III[1,2,3], Zachary J G Gardner[1,2,3], Katherine J Slovik[4], Derek C Liberti[2], Katrina N Estep[2], Wenli Yang[4,5], Qijun Chen[6], Garrett T Santini[3], Javier V Perez[6], Sarah Root[7], Ranvir Bhatia[3], John W Tobias[8], Apoorva Babu[9,10], Michael P Morley[9,10], David B Frank[10,11], Edward E Morrisey[4,9,10], Christopher J Lengner[4,12,*], F. Brad Johnson[6,4,13*]

[1] Medical Scientist Training Program, Perelman School of Medicine, University of Pennsylvania, Philadelphia, PA 19104, USA
[2] Cell and Molecular Biology Graduate Group, Perelman School of Medicine, University of Pennsylvania, Philadelphia, PA 19104, USA
[3] Perelman School of Medicine, University of Pennsylvania, Philadelphia, PA 19104, USA
[4] Institute for Regenerative Medicine, University of Pennsylvania, Philadelphia, PA 19104, USA
[5] Department of Medicine, Perelman School of Medicine, University of Pennsylvania, Philadelphia, PA 19104, USA
[6] Department of Pathology and Laboratory Medicine, Perelman School of Medicine, University of Pennsylvania, Philadelphia, PA 19104, USA
[7] College of Arts and Sciences and Vagelos Scholars Program, University of Pennsylvania, Philadelphia, PA 19104, USA
[8] Penn Genomic Analysis Core, Perelman School of Medicine, University of Pennsylvania, Philadelphia, Pennsylvania 19104, USA
[9] Penn Cardiovascular Institute, University of Pennsylvania, Philadelphia, PA, 19104, USA
[10] Penn-CHOP Lung Biology Institute, University of Pennsylvania, Philadelphia, PA, 19104, USA
[11] Division of Pediatric Cardiology, Department of Pediatrics, Children's Hospital of Philadelphia, Philadelphia, PA 19104, USA
[12] Department of Biomedical Sciences, School of Veterinary Medicine, University of Pennsylvania, Philadelphia, PA 19104, USA
[13] Institute on Aging, University of Pennsylvania, Philadelphia, PA 19104, USA

Co-Corresponding Authors (*)

F. Brad Johnson, MD PhD
Room 406, Stellar Chance Laboratories
422 Curie Blvd
Philadelphia, PA 19104
johnsonb@pennmedicine.upenn.edu

Christopher J. Lengner, PhD
Room 390EA, Old Vet
3800 Spruce Street
Philadelphia, PA 19104
lengner@vet.upenn.edu

Summary

Dyskeratosis congenita (DC) is a rare genetic disorder characterized by deficiencies in telomere maintenance leading to very short telomeres and the premature onset of certain age-related diseases, including pulmonary fibrosis (PF). PF is thought to derive from epithelial failure, particularly that of type II alveolar epithelial (AT2) cells, which are highly dependent on Wnt signaling during development and adult regeneration. We use human iPSC-derived AT2 (iAT2) cells to model how short telomeres affect AT2 cells. Cultured DC mutant iAT2 cells accumulate shortened, uncapped telomeres and manifest defects in the growth of alveolospheres, hallmarks of senescence, and apparent defects in Wnt signaling. The GSK3 inhibitor, CHIR99021, which mimics the output of canonical Wnt signaling, enhances telomerase activity and rescues the defects. These findings support further investigation of Wnt agonists as potential therapies for DC related pathologies.

Keywords

Dyskeratosis congenita, Type II alveolar epithelial cells, pulmonary fibrosis, WNT

Introduction

Dyskeratosis congenita (DC) is a rare genetic disorder characterized by bone marrow failure, skin abnormalities, elevated risk of certain cancers, and liver and pulmonary fibrosis (PF). These pathologies are caused by abnormally shortened and uncapped telomeres arising from deficiencies in telomere maintenance, typically due to defects in the action of telomerase. Significant progress has been made in treating the bone marrow failure of DC patients, particularly *via* transplantation, but PF remains a major life-limiting pathology (Agarwal, 2018; Dietz et al., 2011).

PF is a subtype of interstitial pneumonia that is chronic and progressive, replacing the normal lace-like alveolar architecture with patchy, hyperproliferative fibrous tissue (Lederer and Martinez, 2018). Current therapies are only modestly effective and do not reverse the underlying fibrosis, and lung transplantation is not always an option (King et al., 2014; Lederer and Martinez, 2018; Richeldi et al., 2014; Valapour et al., 2020). While much of the early work in PF pathogenesis focused on unraveling the contributions of fibroblasts, genetic studies of families with a predisposition to PF argue that defects in alveolar epithelial cells and telomeres are key drivers of disease (Alder et al., 2015; Armanios et al., 2007; Bullard et al., 2005; Cogan et al., 2015; Haschek and Witschi, 1979; Kropski et al., 2015; Maitra et al., 2010; Thomas et al., 2002; Wang et al., 2009). Recent work in mice shows that dysfunctional AT2 cells, the putative stem cells of alveoli (Barkauskas et al., 2013), can lead to a progressive chronic fibrotic response similar to that seen in patients (Nureki et al., 2018). Furthermore, many of the same genes which when mutated cause DC have also been linked to familial PF (Alder et al., 2015; Armanios et al., 2007; Cogan et al., 2015; Kropski et al., 2017). In sporadic PF, both age and short telomeres are risk factors, and these risks are linked because age is associated with telomere shortening in the lung, particularly in AT2 cells (Alder et al., 2008; Everaerts et al., 2018). Consistent with a role for telomere dysfunction in driving PF, AT2 cells in sporadic PF express hallmarks of senescence and have shorter telomeres in fibrotic regions than those in non-

fibrotic regions (Disayabutr et al., 2016; Kropski et al., 2015; Snetselaar et al., 2017). Additionally, two human Mendelian randomization studies argue that short telomeres are a cause of PF (Duckworth et al., 2020; Telomeres Mendelian Randomization Collaboration et al., 2017). Murine studies also argue that telomere dysfunction and senescence in AT2 cells can drive PF (Naikawadi et al., 2016; Povedano et al., 2015; Yao et al., 2020). Although causality is thus evident, exactly how AT2 cell telomere dysfunction leads to PF is poorly understood.

Previous work in our lab using mouse and human iPS-derived organoid models of DC intestinal defects uncovered a positive feedback loop by which telomere capping and canonical Wnt signaling support one another under normal conditions to maintain the intestinal stem cell niche (Woo et al., 2016; Yang et al., 2017). In the setting of telomere dysfunction, this virtuous cycle becomes vicious: the resulting suppression of Wnt signaling interferes with stem cell function directly and it also amplifies telomere dysfunction by diminishing Wnt-dependent expression of telomere maintenance factors, including the catalytic subunit of telomerase, TERT, and several of the telomere-protective shelterins. These studies demonstrated that Wnt pathway agonists can rescue these defects, raising the possibility that Wnt agonism could be of therapeutic benefit in DC. Given how telomere dysfunction in AT2 cells appears to drive PF, we wondered if Wnt agonism might be of benefit in pulmonary fibrosis. Wnt signaling is important for lung epithelial cell development (Frank et al., 2016; Goss et al., 2009; Li et al., 2002, 2005; Maretto et al., 2003; Okubo and Hogan, 2004; Ostrin et al., 2018; Shu et al., 2005) and regeneration of the adult lung in response to injury (Nabhan et al., 2018; Zacharias et al., 2018). On the one hand, there is evidence that WNTs may drive PF; for example they have been found to be upregulated in patients with pulmonary fibrosis (Chilosi et al., 2003; Königshoff et al., 2008, 2009). On the other hand, when the canonical Wnt transcriptional effector β-catenin is deleted in AT2 cells, mice are sensitized to bleomcyin induced PF (Tanjore et al., 2013). Wnt signaling is complex and context dependent (Wiese et al., 2018), and the exact spatial, temporal

and cell type-specificity of Wnt signaling in PF remains an area of intense investigation. It is difficult to extrapolate from observational pathologic studies of fully developed PF to the potential functional impact of WNTs at earlier stages of the disease, and the large number of interacting cell types in PF lungs also makes it challenging to identify primary drivers in such studies. Furthermore, differences between mouse and human telomere biology together with the generally lower susceptibility of mice to PF makes mouse modeling difficult. We therefore generated AT2 cell organoids by directed differentiation of human iPSCs (iAT2 cells) to explore how telomere dysfunction might impact their function (Jacob et al., 2017, 2019).

By comparing iAT2s that are isogenic except for an introduced mutation in the gene most often mutated in DC, X-linked *DKC1*, we show that mutant iAT2 cells become senescent in concert with telomere shortening and uncapping. iAT2 cells with short, uncapped telomeres exhibit gene expression changes consistent with decreased Wnt signaling, and treatment with GSK3 inhibitors, such as CHIR99021, rescues their growth and telomere dysfunction. These findings raise the possibility that Wnt agonists may be of benefit in rescuing the stem cell and telomere defects of AT2 cells associated with PF in DC patients.

Results

Engineering a *DKC1* mutation into iPS cells

To model the AT2 cells from DC patients, we engineered a well characterized, causal DC mutation in *DKC1* (*DKC1 A386T*) (Agarwal et al., 2010; Batista et al., 2011; Woo et al., 2016) into the BU3 *NKX2.1::GFP SFTPC::TdTomato (NGST*) human iPS cell line (Jacob et al., 2017). We established an isogenic pair of cell lines: an introduced mutant line and a corresponding wild-type line (Figure S1). Both iPS lines maintained markers of pluripotency and normal karyotypes after the introduction of the *DKC1 A386T* mutation (Figure S1).

Previous work (Agarwal et al., 2010; Batista et al., 2011; Woo et al., 2016) established that iPS cells with the *DKC1 A386T* mutation exhibit decreased telomerase activity resulting in telomere shortening with passage. We confirmed that telomerase activity was reduced, and telomeres shortened with successive passages, in the BU3 *NGST DKC1 A386T* iPS cell line when compared to its wild-type control (Figure S2A-C).

iAT2 cells with short telomeres fail to form alveolospheres and grow in size

We next differentiated these paired iPS cell lines into iAT2 cells using the protocol developed by Jacob et al. (See Figure 1A for differentiation strategy, Figure S3A-B for representative sorting strategies). Using iPSCs 25 passages after the introduction of the mutation initially yielded iAT2s that grew in a similar fashion to wild type, but which developed a growth defect characterized by lower alveolosphere formation efficiency as well as smaller alveolospheres. The phenotype became apparent by 50 days of culture (D50) and was dramatic by D70 (Figure 1A-C). In contrast, using iPSCs only five passages after the introduction of the mutation yielded iAT2s without any defects in alveolosphere growth or size at D70 (Figure S3C). These data indicate that the defects observed were due to progressive telomere shortening after introducing the *DKC1* mutation, and not the immediate effects of telomerase deficiency (or other potential deficiencies) caused by the *DKC1 A386T* mutation *per se*.

Surfactant protein C (SFTPC) is a highly specific marker of AT2 cells (Kalina et al., 1992), and the yield of *SFTPC::TdTomato*+ (*SFTPC+)* cells was reduced significantly at D70 in *DKC1* mutant cultures, while the percentage of *SFTPC*+ cells generated at each time point was not different, suggesting that there is a defect in AT2 cell proliferation or survival (Figure 1D). Sorted *SFTPC*+ cells from iAT2 cell alveolospheres maintained expression of multiple AT2 specific genes suggesting that the introduced mutation did not affect lineage specification (Figure 1E). Thus, DC iPS cells can

generate iAT2 cell alveolospheres, however these alveolospheres lose the capacity to self-renew with successive passaging.

DC iAT2 cells develop hallmarks of senescence at late passage (D70)

To better understand the AT2 cell defects, we further compared the wild type and mutant iAT2 alveolospheres at different passages. Gene expression over successive passages of sorted *SFTPC*+ cells from iAT2 alveolospheres showed decreases in proliferation markers (*MKI67* and *MCM2*) as well as an increase in expression of the cell cycle inhibitor *CDKN1A* (p21), and these changes were most pronounced in mutant alveolospheres (Figure 2A). D70 mutant iAT2 alveolospheres showed an increase in DNA damage marked by 53BP1 foci (Figure 2B), and an increased fraction of cells expressing p21 protein (Figure 2C), but no increase in apoptosis (Figure S3E). Measuring telomere length using qPCR, DC and WT iAT2 cells showed no significant change in average telomere length with passage, although average telomere lengths in mutants trended shorter than in WT (Figure S3F). However, measuring telomere lengths using TeSLA (Lai et al., 2017), which is more sensitive for the detection of short telomeres than most other techniques, revealed that DC iAT2 cells had a preponderance of short telomeres at D70 (Figure 2E-F). Consistent with this, DC iAT2 alveolospheres showed an increased number of telomere dysfunction induced foci (TIFs), a hallmark of uncapped telomeres (i.e. telomeres that signal DNA damage responses and cell cycle checkpoint arrest (Takai et al., 2003) (Figure 2D). These findings indicate that the short and uncapped telomeres that accumulate with passage of DC iAT2 cells lead them to senesce.

RNA-seq reveals pathways differentially expressed in DC iAT2 cells, including those related to Wnt signaling.

To further understand changes in the DC iAT2 cells, we measured the gene expression of sorted SFTPC+ iAT2 cells using RNA-seq (Figure 3A). We found very few significantly differentially expressed genes when comparing wild type and mutant cells at D28 and D50, but a large number of differentially expressed genes at D70 (Figure 3B), arguing that the gene expression changes seen at

D70 are likely driven by uncapped telomeres. Gene Set Enrichment Analyses (GSEA) and Ingenuity Pathway Analysis (IPA) revealed an upregulation of the DNA damage response, the unfolded protein response (UPR), mitochondrial related functions (oxidative phosphorylation, the respiratory electron chain) and a downregulation of hypoxia related signaling, and hedgehog signaling along with other changes (See TableS2 for a full list). IPA analysis revealed similar changes as well as defects in multiple pathways controlled by inflammatory cytokines like IL1β, IL6, IL17 and others (See TableS3 for the full lists). We found a marked upregulation in DC iAT2 cells of many pathways associated with pulmonary fibrosis (Table S1 for curated list of IPF related pathways, see Table S2-S3 for unedited analysis). These included the UPR (Lawson et al., 2008; Mulugeta et al., 2005), thyroid hormone metabolism (Yu et al., 2018), p53 signaling (Shetty et al., 2017), mitochondrial dysfunction and mitophagy (Chung et al., 2019; Yu et al., 2018), and caveolin function (Wang et al., 2006). This analysis also showed an upregulation of non-canonical Wnt signaling (Figure 3C), which correlated with a significant upregulation in *WNT5A* and *WNT11*, known non-canonical Wnt ligands (Figure 3D). Furthermore, almost every *FZD* gene, encoding co-receptors for canonical Wnt signaling, was down regulated in DC iAT2 cells (Figure 3E). Also, GSEA analysis found genes with TCF7 targets in their promoters are downregulated in DC iAT2 cells at D70 (Figure 3F). IPA of master regulators at D70 revealed a decrease in genes controlled by lithium chloride (which can potentiate Wnt signaling) and TCF7 along with an upregulation of genes usually stimulated by Wnt pathway inhibitors (Figure 3G). GSEA also revealed a significant downregulation of targets of miR34a, a miRNA that we previously demonstrated negatively regulates many components of the Wnt pathway in response to uncapped telomeres (Figure 3H) (Yang et al., 2017). The genes encoding four of the six shelterins, proteins that bind and help maintain normal telomere function, are direct targets of the canonical Wnt transcriptional effector β-catenin, and two of these, *TINF2* and *POT1,* were downregulated in D70 DC iAT2 cells, which may contribute to telomere uncapping beyond simple telomere shortening (Figure 3I) (Yang et al., 2017). These data indicate that Wnt signaling in AT2 cells is greatly affected by

shortened telomeres and that non-canonical Wnt signaling may be elevated while canonical (β-catenin-dependent) signaling may be diminished.

GSK3 inhibitors rescues the growth of DC iAT2 alveolospheres

Given our previous work showing that GSK3 inhibition reverses telomere dysfunction and associated defects in intestinal models of DC, we attempted to rescue the DC iAT2 alveolosphere formation defect by treatment with CHIR99021, a well characterized GSK3 inhibitor, which stabilizes β-catenin and upregulates canonical Wnt target genes (Figure 4A). CHIR99021 rescued the alveolosphere growth defect of iAT2 cells in a dose dependent fashion (Figure 4B-C). Furthermore, if alveolospheres were cultured continuously prior to D70 with CHIR99021, this prevented the growth defect from emerging (Figure S4A-B). We also tested another GSK3 inhibitor, CHIR98014, which similarly rescued growth of the mutant iAT2 cells (Figure S4C). These findings suggest that GSK3 inhibition rescued the growth of DC iAT2 alveolospheres.

CHIR99021 downregulates senescence markers and resolves TIFs in DC iAT2 alveolospheres

We ultimately investigated how CHIR99021 affects the telomere status of DC iAT2s. CHIR treated iAT2 cells showed fewer cells with 53BP1 foci, fewer p21+ cells and fewer TIF+ cells (Figure 4D-F). TeSLA revealed no apparent changes in average telomere length or in the frequency of shortest detectable telomeres (Figure S4D-E). However, iAT2 cell telomerase activity was increased in mutant cells treated with CHIR99021 to levels that, remarkably, were even higher than seen in WT cells (Figure 4G). Together, these data argue that GSK3 inhibition not only rescues the growth of DC iAT2 cells, but it also rescues telomere defects, most likely through upregulation of telomerase activity that could extend and recap telomeres that are shorter than those that can be detected by TeSLA.

Discussion

We used isogenic human iPS cell lines to generate DC mutant iAT2 cells with shortened telomeres to interrogate how telomere dysfunction can affect AT2 cell function. We found that shortened and

uncapped telomeres are associated with a defect in alveolosphere formation by iAT2 cells. This defect is characterized by senescent iAT2 cells that upregulate many pathways associated with pulmonary fibrosis including the UPR, mitochondrial biogenesis and function, thyroid hormone signaling, and p53 signaling. DC mutant iAT2 cells also suppress canonical Wnt signaling, and consistent with this, GSK3 inhibition rescues telomerase activity, telomere capping, and alveolosphere formation. This system provides a new preclinical model to better understand PF pathogenesis and how potential new PF therapeutics affect AT2 cell function in the context of telomere dysfunction.

Wnt signaling is a complex pathway, broken down into two major categories: β-catenin dependent (canonical) signaling and β-catenin independent (non-canonical) signaling. These distinctions can also be blurred as evidenced by studies that show how non-canonical ligands, such as *WNT5A*, can activate both arms of Wnt signaling(van Amerongen et al., 2012; Mikels and Nusse, 2006). These complexities therefore make the conflicting reports about whether β-catenin dependent Wnt signaling is of benefit (Tanjore et al., 2013) or of harm in pulmonary fibrosis (Douglas et al., 2006; Henderson et al., 2010; Kim et al., 2011; Königshoff et al., 2008; McDonough et al., 2019) unsurprising. Given the heterogeneity of the disease both in space and time and the context dependence of Wnt signaling, these studies can often only capture a snapshot of the fibrotic response. Furthermore, there are clear differences between mice and humans with regard to telomere and lung biology (Basil and Morrisey, 2020; Gomes et al., 2011). These limitations highlight the need for human models capable of assessing the spatial, temporal, and cell type specific properties of Wnt signaling in PF pathogenesis.

Our study also provides evidence of upregulation of β-catenin-independent signaling in DC iAT2 cells and that re-activating β-catenin dependent Wnt signaling using GSK3 inhibitors might provide support

for AT2 cell proliferation in the context of telomere dysfunction. It is tempting to extrapolate from other models of lung disease to understand how the activity of the β-catenin dependent Wnt pathway might be of benefit in pulmonary fibrosis. β-catenin dependent Wnt signaling improved regeneration and survival in a model of emphysema (Kneidinger et al., 2011), and inhibition of *WNT5A*, and thus presumably some component of β-catenin independent Wnt signaling, improved repair in a model of COPD (Baarsma et al., 2017). Our work, consistent with previous studies, argues that β-catenin dependent Wnt signaling supports AT2 cell telomere capping and proliferation, which may of benefit during regeneration and repair (Nabhan et al., 2018; Uhl et al., 2015; Zacharias et al., 2018).

Our previous work uncovered a positive feedback loop between Wnt signaling and telomeres in the intestine (Woo et al., 2016; Yang et al., 2017). Here we show that aspects of the Wnt-telomere feedback loop appear to be at play in AT2 cells (Fernandez and Johnson, 2018), arguing that this connection between Wnt and telomeres is present not just in proliferative tissues such as the intestine, but also in lung cells, cells from a tissue that are normally quiescent but proliferate in response to injury. Previous work highlighted the importance of telomerase during alveolar regeneration (Driscoll et al., 2000; Lee et al., 2009). Furthermore, given previous demonstrations that *TERT* expression and telomerase activity can be stimulated by Wnt (Hoffmeyer et al., 2012; Jaitner et al., 2012; Zhang et al., 2012), we expected an upregulation of telomerase activity in iAT2 cells when treated with GSK3 inhibitors. However, we did not anticipate the enhanced responsiveness of DC iAT2 cells to CHIR99021. Although we have not explored the underlying mechanism, these findings suggest that cells with compromised telomere maintenance can prime themselves to upregulate telomerase.

This Wnt-telomere feedback loop might not be the only regulatory loop at play in AT2 cells. Given our evidence of upregulation of mitochondrial processes in DC iAT2 cells and how telomere dysfunction

can drive mitochondrial dysfunction (Sahin et al., 2011) and how mitochondrial dysfunction can drive telomere dysfunction (Guha et al., 2018; Passos et al., 2007; Qian et al., 2019), we hypothesize that telomeres might be an integrator of multiple cellular stress responses. Furthermore, our finding of the upregulation of genes associated with the UPR argues that telomere dysfunction could drive the UPR. Many reports have described connections between senescence, a usual consequence of telomere dysfunction, and the UPR (Pluquet et al., 2015) and we hypothesize that the UPR might in turn drive telomere dysfunction. These multiple integrated loops might help explain how these various vital cellular processes combine to cause dysfunction in AT2 cells in PF (Katzen and Beers, 2020).

Recent work, using mouse AT2 cell organoids, has elucidated a developmental trajectory by which AT2 cells can differentiate *via* an intermediate state into type I alveolar epithelial (AT1) cells in response to bleomycin injury (Choi et al., 2020; Kobayashi et al., 2020; Strunz et al., 2020). Of note, the intermediate cells are characterized by high levels of p53 signaling and DNA damage which resolves with their final transition to an AT1 cell fate (Kobayashi et al., 2020), arguing that repairing DNA damage, potentially at telomeres, is an important step in the transition to an AT1 cell. Furthermore, many of the pathways that promote the differentiation of AT2 cells into AT1 cells are downregulated in DC iAT2 cells, including those involving IL1β, glycolysis, and HIF1α (Choi et al., 2020). We speculate that DC AT2 cells with short uncapped telomeres may have trouble suppressing DNA damage at telomeres and therefore in differentiating into AT1 cells during regeneration, perhaps thus contributing to fibrosis. Testing this idea in the human iPSC-derived alveolosphere model will require technical advances to enable the generation of AT1 cells. Regardless, our DC iAT2 cell model recapitulates many hallmarks of PF AT2 cells and offers a new system to probe the underlying biology of PF.

References

Agarwal, S. (2018). Evaluation and Management of Hematopoietic Failure in Dyskeratosis Congenita. Hematol. Oncol. Clin. North Am. *32*, 669–685.

Agarwal, S., Loh, Y.-H., McLoughlin, E.M., Huang, J., Park, I.-H., Miller, J.D., Huo, H., Okuka, M., Dos Reis, R.M., Loewer, S., et al. (2010). Telomere elongation in induced pluripotent stem cells from dyskeratosis congenita patients. Nature *464*, 292–296.

Alder, J.K., Chen, J.J.-L., Lancaster, L., Danoff, S., Su, S.-C., Cogan, J.D., Vulto, I., Xie, M., Qi, X., Tuder, R.M., et al. (2008). Short telomeres are a risk factor for idiopathic pulmonary fibrosis. Proc. Natl. Acad. Sci. U. S. A. *105*, 13051–13056.

Alder, J.K., Stanley, S.E., Wagner, C.L., Hamilton, M., Hanumanthu, V.S., and Armanios, M. (2015). Exome sequencing identifies mutant TINF2 in a family with pulmonary fibrosis. Chest *147*, 1361–1368.

van Amerongen, R., Fuerer, C., Mizutani, M., and Nusse, R. (2012). Wnt5a can both activate and repress Wnt/β-catenin signaling during mouse embryonic development. Dev. Biol. *369*, 101–114.

Armanios, M.Y., Chen, J.J.-L., Cogan, J.D., Alder, J.K., Ingersoll, R.G., Markin, C., Lawson, W.E., Xie, M., Vulto, I., Phillips, J.A., et al. (2007). Telomerase mutations in families with idiopathic pulmonary fibrosis. N. Engl. J. Med. *356*, 1317–1326.

Baarsma, H.A., Skronska-Wasek, W., Mutze, K., Ciolek, F., Wagner, D.E., John-Schuster, G., Heinzelmann, K., Günther, A., Bracke, K.R., Dagouassat, M., et al. (2017). Noncanonical WNT-5A signaling impairs endogenous lung repair in COPD. J. Exp. Med. *214*, 143–163.

Barkauskas, C.E., Cronce, M.J., Rackley, C.R., Bowie, E.J., Keene, D.R., Stripp, B.R., Randell, S.H., Noble, P.W., and Hogan, B.L.M. (2013). Type 2 alveolar cells are stem cells in adult lung. J. Clin. Invest. *123*, 3025–3036.

Basil, M.C., and Morrisey, E.E. (2020). Lung regeneration: a tale of mice and men. Semin. Cell Dev. Biol. *100*, 88–100.

Batista, L.F.Z., Pech, M.F., Zhong, F.L., Nguyen, H.N., Xie, K.T., Zaug, A.J., Crary, S.M., Choi, J., Sebastiano, V., Cherry, A., et al. (2011). Telomere shortening and loss of self-renewal in dyskeratosis congenita induced pluripotent stem cells. Nature *474*, 399–402.

Bullard, J.E., Wert, S.E., Whitsett, J.A., Dean, M., and Nogee, L.M. (2005). ABCA3 mutations associated with pediatric interstitial lung disease. Am. J. Respir. Crit. Care Med. *172*, 1026–1031.

Cawthon, R.M. (2002). Telomere measurement by quantitative PCR. Nucleic Acids Res. *30*, e47.

Chilosi, M., Poletti, V., Zamò, A., Lestani, M., Montagna, L., Piccoli, P., Pedron, S., Bertaso, M., Scarpa, A., Murer, B., et al. (2003). Aberrant Wnt/beta-catenin pathway activation in idiopathic pulmonary fibrosis. Am. J. Pathol. *162*, 1495–1502.

Choi, J., Park, J.-E., Tsagkogeorga, G., Yanagita, M., Koo, B.-K., Han, N., and Lee, J.-H. (2020). Inflammatory Signals Induce AT2 Cell-Derived Damage-Associated Transient Progenitors that Mediate Alveolar Regeneration. Cell Stem Cell.

Chung, K.-P., Hsu, C.-L., Fan, L.-C., Huang, Z., Bhatia, D., Chen, Y.-J., Hisata, S., Cho, S.J., Nakahira, K., Imamura, M., et al. (2019). Mitofusins regulate lipid metabolism to mediate the development of lung fibrosis. Nat. Commun. *10*, 3390.

Cogan, J.D., Kropski, J.A., Zhao, M., Mitchell, D.B., Rives, L., Markin, C., Garnett, E.T., Montgomery, K.H., Mason, W.R., McKean, D.F., et al. (2015). Rare variants in RTEL1 are associated with familial interstitial pneumonia. Am. J. Respir. Crit. Care Med. *191*, 646–655.

Dietz, A.C., Orchard, P.J., Baker, K.S., Giller, R.H., Savage, S.A., Alter, B.P., and Tolar, J. (2011). Disease-specific hematopoietic cell transplantation: nonmyeloablative conditioning regimen for dyskeratosis congenita. Bone Marrow Transplant. *46*, 98–104.

Disayabutr, S., Kim, E.K., Cha, S.-I., Green, G., Naikawadi, R.P., Jones, K.D., Golden, J.A., Schroeder, A., Matthay, M.A., Kukreja, J., et al. (2016). miR-34 miRNAs Regulate Cellular Senescence in Type II Alveolar Epithelial Cells of Patients with Idiopathic Pulmonary Fibrosis. PLoS One *11*, e0158367.

Dolgalev, I. (2020). msigdbr: MSigDB Gene Sets for Multiple Organisms in a Tidy Data Format.

Douglas, I.S., Diaz del Valle, F., Winn, R.A., and Voelkel, N.F. (2006). Beta-catenin in the fibroproliferative response to acute lung injury. Am. J. Respir. Cell Mol. Biol. *34*, 274–285.

Driscoll, B., Buckley, S., Bui, K.C., Anderson, K.D., and Warburton, D. (2000). Telomerase in alveolar epithelial development and repair. Am. J. Physiol. Lung Cell. Mol. Physiol. *279*, L1191–L1198.

Duckworth, A., Gibbons, M.A., Allen, R.J., Almond, H., Beaumont, R.N., Wood, A.R., Lunnon, K.R., Lindsay, M.A., Wain, L.V., Tyrrell, J., et al. (2020). Evidence that telomere length is causal for Idiopathic Pulmonary Fibrosis but not Chronic Obstructive Pulmonary Disease: A Mendelian Randomisation Study (medRxiv).

Everaerts, S., Lammertyn, E.J., Martens, D.S., De Sadeleer, L.J., Maes, K., van Batenburg, A.A., Goldschmeding, R., van Moorsel, C.H.M., Dupont, L.J., Wuyts, W.A., et al. (2018). The aging lung: tissue telomere shortening in health and disease. Respir. Res. *19*, 95.

Fernandez, R.J., 3rd, and Johnson, F.B. (2018). A regulatory loop connecting WNT signaling and telomere capping: possible therapeutic implications for dyskeratosis congenita. Ann. N. Y. Acad. Sci. *1418*, 56–68.

Frank, D.B., Peng, T., Zepp, J.A., Snitow, M., Vincent, T.L., Penkala, I.J., Cui, Z., Herriges, M.J., Morley, M.P., Zhou, S., et al. (2016). Emergence of a Wave of Wnt Signaling that Regulates Lung Alveologenesis by Controlling Epithelial Self-Renewal and Differentiation. Cell Rep. *17*, 2312–2325.

Gomes, N.M.V., Ryder, O.A., Houck, M.L., Charter, S.J., Walker, W., Forsyth, N.R., Austad, S.N., Venditti, C., Pagel, M., Shay, J.W., et al. (2011). Comparative biology of mammalian telomeres: hypotheses on ancestral states and the roles of telomeres in longevity determination. Aging Cell *10*, 761–768.

Goss, A.M., Tian, Y., Tsukiyama, T., Cohen, E.D., Zhou, D., Lu, M.M., Yamaguchi, T.P., and Morrisey, E.E. (2009). Wnt2/2b and beta-catenin signaling are necessary and sufficient to specify lung progenitors in the foregut. Dev. Cell *17*, 290–298.

Guha, M., Srinivasan, S., Johnson, F.B., Ruthel, G., Guja, K., Garcia-Diaz, M., Kaufman, B.A., Glineburg, M.R., Fang, J., Nakagawa, H., et al. (2018). hnRNPA2 mediated acetylation reduces telomere length in response to mitochondrial dysfunction. PLoS One *13*, e0206897.

Hadley Wickham, J.B. (2019). readxl: Read Excel Files.

Haschek, W.M., and Witschi, H. (1979). Pulmonary fibrosis--a possible mechanism. Toxicol. Appl. Pharmacol. *51*, 475–487.

Henderson, W.R., Jr, Chi, E.Y., Ye, X., Nguyen, C., Tien, Y.-T., Zhou, B., Borok, Z., Knight, D.A., and Kahn, M. (2010). Inhibition of Wnt/beta-catenin/CREB binding protein (CBP) signaling reverses pulmonary fibrosis. Proc. Natl. Acad. Sci. U. S. A. *107*, 14309–14314.

Herbert, B.-S., Hochreiter, A.E., Wright, W.E., and Shay, J.W. (2006). Nonradioactive detection of telomerase activity using the telomeric repeat amplification protocol. Nat. Protoc. *1*, 1583–1590.

Hoffmeyer, K., Raggioli, A., Rudloff, S., Anton, R., Hierholzer, A., Del Valle, I., Hein, K., Vogt, R., and Kemler, R. (2012). Wnt/β-catenin signaling regulates telomerase in stem cells and cancer cells. Science *336*, 1549–1554.

Jacob, A., Morley, M., Hawkins, F., McCauley, K.B., Jean, J.C., Heins, H., Na, C.-L., Weaver, T.E., Vedaie, M., Hurley, K., et al. (2017). Differentiation of Human Pluripotent Stem Cells into Functional Lung Alveolar Epithelial Cells. Cell Stem Cell *21*, 472–488.e10.

Jacob, A., Vedaie, M., Roberts, D.A., Thomas, D.C., Villacorta-Martin, C., Alysandratos, K.-D., Hawkins, F., and Kotton, D.N. (2019). Derivation of self-renewing lung alveolar epithelial type II cells from human pluripotent stem cells. Nat. Protoc.

Jaitner, S., Reiche, J.A., Schäffauer, A.J., Hiendlmeyer, E., Herbst, H., Brabletz, T., Kirchner, T., and Jung, A. (2012). Human telomerase reverse transcriptase (hTERT) is a target gene of β-catenin in human colorectal tumors. Cell Cycle *11*, 3331–3338.

Joglekar, M.V., Satoor, S.N., Wong, W.K.M., Cheng, F., Ma, R.C.W., and Hardikar, A.A. (2020). An Optimised Step-by-Step Protocol for Measuring Relative Telomere Length. Methods Protoc *3*.

Kalina, M., Mason, R.J., and Shannon, J.M. (1992). Surfactant protein C is expressed in alveolar type II cells but not in Clara cells of rat lung. Am. J. Respir. Cell Mol. Biol. *6*, 594–600.

Katzen, J., and Beers, M.F. (2020). Contributions of alveolar epithelial cell quality control to pulmonary fibrosis. J. Clin. Invest. *130*, 5088–5099.

Kim, T.H., Kim, S.-H., Seo, J.-Y., Chung, H., Kwak, H.J., Lee, S.-K., Yoon, H.J., Shin, D.H., Park, S.S., and Sohn, J.W. (2011). Blockade of the Wnt/β-catenin pathway attenuates bleomycin-induced pulmonary fibrosis. Tohoku J. Exp. Med. *223*, 45–54.

Kimura, M., Stone, R.C., Hunt, S.C., Skurnick, J., Lu, X., Cao, X., Harley, C.B., and Aviv, A. (2010). Measurement of telomere length by the Southern blot analysis of terminal restriction fragment lengths. Nat. Protoc. *5*, 1596–1607.

King, T.E., Jr, Bradford, W.Z., Castro-Bernardini, S., Fagan, E.A., Glaspole, I., Glassberg, M.K., Gorina, E., Hopkins, P.M., Kardatzke, D., Lancaster, L., et al. (2014). A phase 3 trial of pirfenidone in patients with idiopathic pulmonary fibrosis. N. Engl. J. Med. *370*, 2083–2092.

Kneidinger, N., Yildirim, A.Ö., Callegari, J., Takenaka, S., Stein, M.M., Dumitrascu, R., Bohla, A., Bracke, K.R., Morty, R.E., Brusselle, G.G., et al. (2011). Activation of the WNT/β-catenin pathway attenuates experimental emphysema. Am. J. Respir. Crit. Care Med. *183*, 723–733.

Kobayashi, Y., Tata, A., Konkimalla, A., Katsura, H., Lee, R.F., Ou, J., Banovich, N.E., Kropski, J.A., and Tata, P.R. (2020). Persistence of a regeneration-associated, transitional alveolar epithelial cell state in pulmonary fibrosis. Nat. Cell Biol. 1–13.

Königshoff, M., Balsara, N., Pfaff, E.-M., Kramer, M., Chrobak, I., Seeger, W., and Eickelberg, O. (2008). Functional Wnt signaling is increased in idiopathic pulmonary fibrosis. PLoS One *3*, e2142.

Königshoff, M., Kramer, M., Balsara, N., Wilhelm, J., Amarie, O.V., Jahn, A., Rose, F., Fink, L., Seeger, W., Schaefer, L., et al. (2009). WNT1-inducible signaling protein-1 mediates pulmonary fibrosis in mice and is upregulated in humans with idiopathic pulmonary fibrosis. J. Clin. Invest. *119*, 772–787.

Krämer, A., Green, J., Pollard, J., Jr, and Tugendreich, S. (2014). Causal analysis approaches in Ingenuity Pathway Analysis. Bioinformatics *30*, 523–530.

Kropski, J.A., Pritchett, J.M., Zoz, D.F., Crossno, P.F., Markin, C., Garnett, E.T., Degryse, A.L., Mitchell, D.B., Polosukhin, V.V., Rickman, O.B., et al. (2015). Extensive phenotyping of individuals at risk for familial interstitial pneumonia reveals clues to the pathogenesis of interstitial lung disease. Am. J. Respir. Crit. Care Med. *191*, 417–426.

Kropski, J.A., Reiss, S., Markin, C., Brown, K.K., Schwartz, D.A., Schwarz, M.I., Loyd, J.E., Phillips, J.A., 3rd, Blackwell, T.S., and Cogan, J.D. (2017). Rare Genetic Variants in PARN Are Associated with Pulmonary Fibrosis in Families. Am. J. Respir. Crit. Care Med. *196*, 1481–1484.

Lai, T.-P., Wright, W.E., and Shay, J.W. (2016). Generation of digoxigenin-incorporated probes to enhance DNA detection sensitivity. Biotechniques *60*, 306–309.

Lai, T.-P., Zhang, N., Noh, J., Mender, I., Tedone, E., Huang, E., Wright, W.E., Danuser, G., and Shay, J.W. (2017). A method for measuring the distribution of the shortest telomeres in cells and tissues. Nat. Commun. *8*, 1356.

Lawson, W.E., Crossno, P.F., Polosukhin, V.V., Roldan, J., Cheng, D.-S., Lane, K.B., Blackwell, T.R., Xu, C., Markin, C., Ware, L.B., et al. (2008). Endoplasmic reticulum stress in alveolar epithelial cells is prominent in IPF: association with altered surfactant protein processing and herpesvirus infection. Am. J. Physiol. Lung Cell. Mol. Physiol. *294*, L1119–L1126.

Lederer, D.J., and Martinez, F.J. (2018). Idiopathic Pulmonary Fibrosis. N. Engl. J. Med. *378*, 1811–1823.

Lee, J., Reddy, R., Barsky, L., Scholes, J., Chen, H., Shi, W., and Driscoll, B. (2009). Lung alveolar integrity is compromised by telomere shortening in telomerase-null mice. Am. J. Physiol. Lung Cell. Mol. Physiol. *296*, L57–L70.

Li, C., Xiao, J., Hormi, K., Borok, Z., and Minoo, P. (2002). Wnt5a participates in distal lung morphogenesis. Dev. Biol. *248*, 68–81.

Li, C., Hu, L., Xiao, J., Chen, H., Li, J.T., Bellusci, S., Delanghe, S., and Minoo, P. (2005). Wnt5a regulates Shh and Fgf10 signaling during lung development. Dev. Biol. *287*, 86–97.

Liberzon, A., Subramanian, A., Pinchback, R., Thorvaldsdóttir, H., Tamayo, P., and Mesirov, J.P. (2011). Molecular signatures database (MSigDB) 3.0. Bioinformatics *27*, 1739–1740.

Liberzon, A., Birger, C., Thorvaldsdóttir, H., Ghandi, M., Mesirov, J.P., and Tamayo, P. (2015). The Molecular Signatures Database (MSigDB) hallmark gene set collection. Cell Syst *1*, 417–425.

Love, M.I., Huber, W., and Anders, S. (2014). Moderated estimation of fold change and dispersion for RNA-seq data with DESeq2. Genome Biol. *15*, 550.

Maitra, M., Wang, Y., Gerard, R.D., Mendelson, C.R., and Garcia, C.K. (2010). Surfactant protein A2 mutations associated with pulmonary fibrosis lead to protein instability and endoplasmic reticulum stress. J. Biol. Chem. *285*, 22103–22113.

Maretto, S., Cordenonsi, M., Dupont, S., Braghetta, P., Broccoli, V., Hassan, A.B., Volpin, D., Bressan, G.M., and Piccolo, S. (2003). Mapping Wnt/β-catenin signaling during mouse development and in colorectal tumors. Proc. Natl. Acad. Sci. U. S. A. *100*, 3299–3304.

McDonough, J.E., Ahangari, F., Li, Q., Jain, S., Verleden, S.E., Herazo-Maya, J., Vukmirovic, M., DeIuliis, G., Tzouvelekis, A., Tanabe, N., et al. (2019). Transcriptional regulatory model of fibrosis progression in the human lung. JCI Insight *4*.

Mikels, A.J., and Nusse, R. (2006). Purified Wnt5a protein activates or inhibits beta-catenin-TCF signaling depending on receptor context. PLoS Biol. *4*, e115.

Mulugeta, S., Nguyen, V., Russo, S.J., Muniswamy, M., and Beers, M.F. (2005). A surfactant protein C precursor protein BRICHOS domain mutation causes endoplasmic reticulum stress, proteasome dysfunction, and caspase 3 activation. Am. J. Respir. Cell Mol. Biol. *32*, 521–530.

Nabhan, A.N., Brownfield, D.G., Harbury, P.B., Krasnow, M.A., and Desai, T.J. (2018). Single-cell Wnt signaling niches maintain stemness of alveolar type 2 cells. Science *359*, 1118–1123.

Naikawadi, R.P., Disayabutr, S., Mallavia, B., Donne, M.L., Green, G., La, J.L., Rock, J.R., Looney, M.R., and Wolters, P.J. (2016). Telomere dysfunction in alveolar epithelial cells causes lung remodeling and fibrosis. JCI Insight *1*, e86704.

Nureki, S.-I., Tomer, Y., Venosa, A., Katzen, J., Russo, S.J., Jamil, S., Barrett, M., Nguyen, V., Kopp, M., Mulugeta, S., et al. (2018). Expression of mutant Sftpc in murine alveolar epithelia drives spontaneous lung fibrosis. J. Clin. Invest. *128*, 4008–4024.

Okubo, T., and Hogan, B.L.M. (2004). Hyperactive Wnt signaling changes the developmental potential of embryonic lung endoderm. J. Biol. *3*, 11.

Ostrin, E.J., Little, D.R., Gerner-Mauro, K.N., Sumner, E.A., Ríos-Corzo, R., Ambrosio, E., Holt, S.E., Forcioli-Conti, N., Akiyama, H., Hanash, S.M., et al. (2018). β-Catenin maintains lung epithelial progenitors after lung specification. Development *145*.

Passos, J.F., Saretzki, G., Ahmed, S., Nelson, G., Richter, T., Peters, H., Wappler, I., Birket, M.J., Harold, G., Schaeuble, K., et al. (2007). Mitochondrial dysfunction accounts for the stochastic heterogeneity in telomere-dependent senescence. PLoS Biol. *5*, e110.

Patro, R., Duggal, G., Love, M.I., Irizarry, R.A., and Kingsford, C. (2017). Salmon provides fast and bias-aware quantification of transcript expression. Nat. Methods *14*, 417–419.

Pluquet, O., Pourtier, A., and Abbadie, C. (2015). The unfolded protein response and cellular senescence. A review in the theme: cellular mechanisms of endoplasmic reticulum stress signaling in health and disease. Am. J. Physiol. Cell Physiol. *308*, C415–C425.

Povedano, J.M., Martinez, P., Flores, J.M., Mulero, F., and Blasco, M.A. (2015). Mice with Pulmonary Fibrosis Driven by Telomere Dysfunction. Cell Rep. *12*, 286–299.

Qian, W., Kumar, N., Roginskaya, V., Fouquerel, E., Opresko, P.L., Shiva, S., Watkins, S.C., Kolodieznyi, D., Bruchez, M.P., and Van Houten, B. (2019). Chemoptogenetic damage to mitochondria causes rapid telomere dysfunction. Proc. Natl. Acad. Sci. U. S. A. *116*, 18435–18444.

Richeldi, L., du Bois, R.M., Raghu, G., Azuma, A., Brown, K.K., Costabel, U., Cottin, V., Flaherty, K.R., Hansell, D.M., Inoue, Y., et al. (2014). Efficacy and safety of nintedanib in idiopathic pulmonary fibrosis. N. Engl. J. Med. *370*, 2071–2082.

RStudio Team (2020). RStudio: Integrated Development Environment for R (Boston, MA: RStudio, PBC.).

Sahin, E., Colla, S., Liesa, M., Moslehi, J., Müller, F.L., Guo, M., Cooper, M., Kotton, D., Fabian, A.J., Walkey, C., et al. (2011). Telomere dysfunction induces metabolic and mitochondrial compromise. Nature *470*, 359–365.

Shetty, S.K., Tiwari, N., Marudamuthu, A.S., Puthusseri, B., Bhandary, Y.P., Fu, J., Levin, J., Idell, S., and Shetty, S. (2017). p53 and miR-34a Feedback Promotes Lung Epithelial Injury and Pulmonary Fibrosis. Am. J. Pathol. *187*, 1016–1034.

Shu, W., Guttentag, S., Wang, Z., Andl, T., Ballard, P., Lu, M.M., Piccolo, S., Birchmeier, W., Whitsett, J.A., Millar, S.E., et al. (2005). Wnt/beta-catenin signaling acts upstream of N-myc, BMP4, and FGF signaling to regulate proximal-distal patterning in the lung. Dev. Biol. *283*, 226–239.

Snetselaar, R., van Batenburg, A.A., van Oosterhout, M.F.M., Kazemier, K.M., Roothaan, S.M., Peeters, T., van der Vis, J.J., Goldschmeding, R., Grutters, J.C., and van Moorsel, C.H.M. (2017). Short telomere length in IPF lung associates with fibrotic lesions and predicts survival. PLoS One *12*, e0189467.

Strunz, M., Simon, L.M., Ansari, M., Kathiriya, J.J., Angelidis, I., Mayr, C.H., Tsidiridis, G., Lange, M., Mattner, L.F., Yee, M., et al. (2020). Alveolar regeneration through a Krt8+ transitional stem cell state that persists in human lung fibrosis. Nat. Commun. *11*, 3559.

Subramanian, A., Tamayo, P., Mootha, V.K., Mukherjee, S., Ebert, B.L., Gillette, M.A., Paulovich, A., Pomeroy, S.L., Golub, T.R., Lander, E.S., et al. (2005). Gene set enrichment analysis: a knowledge-based approach for interpreting genome-wide expression profiles. Proc. Natl. Acad. Sci. U. S. A. *102*, 15545–15550.

Suram, A., Kaplunov, J., Patel, P.L., Ruan, H., Cerutti, A., Boccardi, V., Fumagalli, M., Di Micco, R., Mirani, N., Gurung, R.L., et al. (2012). Oncogene-induced telomere dysfunction enforces cellular senescence in human cancer precursor lesions. EMBO J. *31*, 2839–2851.

Takai, H., Smogorzewska, A., and de Lange, T. (2003). DNA damage foci at dysfunctional telomeres. Curr. Biol. *13*, 1549–1556.

Tanjore, H., Degryse, A.L., Crossno, P.F., Xu, X.C., McConaha, M.E., Jones, B.R., Polosukhin, V.V., Bryant, A.J., Cheng, D.-S., Newcomb, D.C., et al. (2013). β-catenin in the alveolar epithelium protects from lung fibrosis after intratracheal bleomycin. Am. J. Respir. Crit. Care Med. *187*, 630–639.

Team, R Core (2020). R: A language and environment for statistical computing (Vienna, Austria: R Foundation for Statistical Computing).

Telomeres Mendelian Randomization Collaboration, Haycock, P.C., Burgess, S., Nounu, A., Zheng, J., Okoli, G.N., Bowden, J., Wade, K.H., Timpson, N.J., Evans, D.M., et al. (2017). Association Between Telomere Length and Risk of Cancer and Non-Neoplastic Diseases: A Mendelian Randomization Study. JAMA Oncol *3*, 636–651.

Thomas, A.Q., Lane, K., Phillips, J., 3rd, Prince, M., Markin, C., Speer, M., Schwartz, D.A., Gaddipati, R., Marney, A., Johnson, J., et al. (2002). Heterozygosity for a surfactant protein C gene mutation associated with usual interstitial pneumonitis and cellular nonspecific interstitial pneumonitis in one kindred. Am. J. Respir. Crit. Care Med. *165*, 1322–1328.

Uhl, F.E., Vierkotten, S., Wagner, D.E., Burgstaller, G., Costa, R., Koch, I., Lindner, M., Meiners, S., Eickelberg, O., and Königshoff, M. (2015). Preclinical validation and imaging of Wnt-induced repair in human 3D lung tissue cultures. Eur. Respir. J. *46*, 1150–1166.

Uphoff, C.C., and Drexler, H.G. (2014). Detection of Mycoplasma contamination in cell cultures. Curr. Protoc. Mol. Biol. *106*, 28.4.1–14.

Valapour, M., Lehr, C.J., Skeans, M.A., Smith, J.M., Uccellini, K., Goff, R., Foutz, J., Israni, A.K., Snyder, J.J., and Kasiske, B.L. (2020). OPTN/SRTR 2018 Annual Data Report: Lung. Am. J. Transplant *20 Suppl s1*, 427–508.

Wang, X.M., Zhang, Y., Kim, H.P., Zhou, Z., Feghali-Bostwick, C.A., Liu, F., Ifedigbo, E., Xu, X., Oury, T.D., Kaminski, N., et al. (2006). Caveolin-1: a critical regulator of lung fibrosis in idiopathic pulmonary fibrosis. J. Exp. Med. *203*, 2895–2906.

Wang, Y., Kuan, P.J., Xing, C., Cronkhite, J.T., Torres, F., Rosenblatt, R.L., DiMaio, J.M., Kinch, L.N., Grishin, N.V., and Garcia, C.K. (2009). Genetic defects in surfactant protein A2 are associated with pulmonary fibrosis and lung cancer. Am. J. Hum. Genet. *84*, 52–59.

Wickham, H., Averick, M., Bryan, J., Chang, W., McGowan, L., François, R., Grolemund, G., Hayes, A., Henry, L., Hester, J., et al. (2019). Welcome to the Tidyverse. JOSS *4*, 1686.

Wiese, K.E., Nusse, R., and van Amerongen, R. (2018). Wnt signalling: conquering complexity. Development *145*.

Woo, D.-H., Chen, Q., Yang, T.-L.B., Glineburg, M.R., Hoge, C., Leu, N.A., Johnson, F.B., and Lengner, C.J. (2016). Enhancing a Wnt-Telomere Feedback Loop Restores Intestinal Stem Cell Function in a Human Organotypic Model of Dyskeratosis Congenita. Cell Stem Cell *19*, 397–405.

Yang, T.-L.B., Chen, Q., Deng, J.T., Jagannathan, G., Tobias, J.W., Schultz, D.C., Wang, S., Lengner, C.J., Rustgi, A.K., Lynch, J.P., et al. (2017). Mutual reinforcement between telomere capping and canonical Wnt signalling in the intestinal stem cell niche. Nat. Commun. *8*, 14766.

Yao, C., Guan, X., Carraro, G., Parimon, T., Liu, X., Huang, G., Mulay, A., Soukiasian, H.J., David, G., Weigt, S.S., et al. (2020). Senescence of Alveolar Type 2 Cells Drives Progressive Pulmonary Fibrosis. Am. J. Respir. Crit. Care Med.

Yihui Xie, J.C.A.X.T. (2020). DT: A Wrapper of the JavaScript Library “DataTables.”

Yu, G. (2020). enrichplot: Visualization of Functional Enrichment Result.

Yu, G., Wang, L.-G., Han, Y., and He, Q.-Y. (2012). clusterProfiler: an R package for comparing biological themes among gene clusters. OMICS *16*, 284–287.

Yu, G., Tzouvelekis, A., Wang, R., Herazo-Maya, J.D., Ibarra, G.H., Srivastava, A., de Castro, J.P.W., DeIuliis, G., Ahangari, F., Woolard, T., et al. (2018). Thyroid hormone inhibits lung fibrosis in mice by improving epithelial mitochondrial function. Nat. Med. *24*, 39–49.

Zacharias, W.J., Frank, D.B., Zepp, J.A., Morley, M.P., Alkhaleel, F.A., Kong, J., Zhou, S., Cantu, E., and Morrisey, E.E. (2018). Regeneration of the lung alveolus by an evolutionarily conserved epithelial progenitor. Nature *555*, 251–255.

Zhang, Y., Toh, L., Lau, P., and Wang, X. (2012). Human telomerase reverse transcriptase (hTERT) is a novel target of the Wnt/β-catenin pathway in human cancer. J. Biol. Chem. *287*, 32494–32511.

Experimental Procedures

iPSc Line Generation and Maintenance

The patient derived AG04646 *DKC1 A386T* line was obtained from our previous studies (Woo et al., 2016). The BU3 *NKX2.1::GFP SFTPC::TdTomato* line was a generous gift from Dr. Darrell Kotton at Boston University. iPS cells used for differentiation were maintained on growth factor reduced Matrigel (Corning) coated plates in StemMACS™ iPS-Brew XF medium (Miltenyi Biotec). Cells were cultured in clusters and passaged every 4-5 days using StemMACS Dissociation reagent (Miltenyi Biotec). All iPS lines were genotyped using an RFLP at the relevant important loci and the sequence was confirmed by Sanger sequencing. All cells were routinely screened for mycoplasma contamination using a PCR based assay (Uphoff and Drexler, 2014).

CRISPR Editing for generating Paired DKC1 Mutant Cell Lines in BU3 NGST

To generate the introduced BU3 NGST line harboring the *DKC1* mutation, we used the CRISPR track on the UCSC genome browser to select candidate guideRNAs (gRNAs) that targeted as close to the individual mutation as possible, had easily mutable PAM sites and would introduce a new restriction site to make screening easier (see the Key Resources Table for exact sequences and Figure S1 for details). gRNAs were ordered as oligos from IDT and cloned into pX458, a gift from Dr. Feng Zhang's lab (Addgene # 48138). The candidate guides were tested for cutting efficiency by transfecting them into HEK293T cells and assaying cutting efficiency using T7E1 digestion of the PCR amplified locus. The most efficient guides were chosen and ssODN HDR templates were designed to eliminate the PAM. iPS cells were then nucleofected with the Amaxa Nucleofection system using the following program (P3, CA-137) (Lonza). The cells were allowed to recover for 36-48 hours at high density in the presence of ROCK inhibitor and then isolated by FACS for GFPhi cells. They were plated at low density (2500 cells/10 cm plate) and allowed to form single colonies. After seven to ten days, individual clones were selected and transferred to 96 well plates, and screened for introduction of the restriction site for each mutation. Restriction enzyme positive clones were expanded and then subjected to sanger sequencing for identification of correctly edited clones. Successfully edited

clones were checked for normal karyotype by G-banding (Cell Line Genetics), mycoplasma contamination, and pluripotency marker expression by immunofluorescence, and were subsequently passaged for at least 5 passages before being re-genotyped to ensure that the clones were not mixed. During differentiations, all iAT2 cells were genotyped by restriction digest to ensure that the mutation was not lost with passage.

Directed differentiation into NKX2.1+ lung progenitors and SFTPC+ iPS-derived AT2 cells

A modified version of the protocol described in (Jacob et al., 2017) was used to generate SFTPC expressing iAT2 cells. In brief, iPS cells were seeded at 500,000 cells per well on a 6-well plate with ROCK inhibitor for 24 hours and incubated at 5% O2 | 5% CO2 | 90% N2. Definitive endoderm was induced using the StemDiff Definitive Endoderm kit for 3 days. Next, the cells were split at a ratio of 1:3 onto fresh Matrigel plates and anteriorized using dorsomorphin (2 μM) and SB431542 (10 μM) in complete Serum Free Differentiation Media (cSFDM) for three days. Cells were then differentiated into NKX2.1+ progenitors by incubating in CBRa media (cSFDM containing CHIR99021 (3 μM), BMP4 (10 ng/mL), and retinoic acid (100 nM)) for 7 days changing media every 2 days at first and then increasing to every day media changes when the media became more acidic. On day 15 or 16, *NKX2.1*+ progenitors were isolated using a FACSJazz sorter using the endogenous *NKX2.1::GFP* reporter.

NKX2.1+ sorted cells were replated at a density of 400,000 cells/mL in 90% Matrigel supplemented with 10% of CK+DCI+TZV media (cSFDM containing 3 μM CHIR99021, 10 ng/mL KGF, 100 nM dexamethasone, 100μM 8Br-cAMP and 100 μM IBMX and 2 μM TZV) (from now on referred to as 90/10 Matrigel). The Matrigel droplets were allowed to cure at 37 °C for 20-30 minutes and then overlaid with an appropriate amount of CK+DCI+TZV Media. These alveolosphere containing matrigel droplets were incubated at 37˚C at 20% O2 | 5% CO2 | 75% N2 (room air) for 14 days changing with fresh media every other day. On Day 28, the iAT2 containing alveolospheres were sorted on a

FACSJazz sorter for SFTPC+ cells using the endogenous SFTPC::TdTomato reporter. These sorted SFTPC+ cells were replated at a concentration of 65,000 cells / mL in 90/10 Matrigel drops and grown in K+DCI+TZV at 37˚C in an ambient air incubator supplemented to 5% CO2 for 3 weeks changing media every other day.

Alveolosphere Counting and Formation Efficiency Calculations

Alveolosphere images were taken on a Leica Thunder widefield microscope using a 1.25x objective. Z-stacks were maximum projected and then thresholded using ImageJ to create a binary file. Binary files were eroded and dilated to ensure maximum determination of the alveolosphere size. Finally the binary images were separated by watershedding and alveolospheres were counted using Analyze Particles in ImageJ.

Immunofluorescence Microscopy of iAT2 alveolospheres

Alveolospheres were washed with PBS and then fixed in place using 2% PFA at room temperature at room temperature for 30 minutes and then dehydrated and paraffin embedded and sectioned. Once cut, slides were de-paraffinized, rehydrated, permeabilized, and antigens were retrieved by steaming for 15 minutes in a citrate buffer (Vector Labs). After blocking, each slide was incubated with a primary antibody using the concentrations listed in the Key Resource Table. Slides were incubated with primary antibody at 37 °C for two hours. After washing, slides were incubated with appropriate fluorochrome conjugated secondary antibodies (see Key Resources Table for antibody details). Slides were then washed, counterstained with DAPI, and mounted. Images were acquired using a Leica Thunder Widefield Microscope.

TIFs were stained as described in (Suram et al., 2012). In brief, cut slides were de-paraffinized, rehydrated, permeabilized and antigens were retrieved as for other immunofluoresence stains. Slides were blocked and stained for 53BP1 and then stained with an appropriate fluorochrome conjugated secondary antibody. Slides were then re-fixed with paraformaldehyde, quenched with glycine, re-dehydrated in an ethanol series, and air dried. The slides were then stained with the PNA probe. The

slides were washed, rehydrated in an ethanol series, and stained with a tertiary fluorochrome conjugated antibody. Slides were then washed, counterstained with DAPI, and mounted. TIF images were acquired using a Leica SP8 Confocal microscope. Quantification of nuclei was carried out in ImageJ in a blinded fashion.

Measurement of Telomerase Activity with TRAP

iPS cells or iAT2 cells were cultured as indicated in each figure legend. 100,000 cells were harvested using methods described and lysed using NP-40 lysis buffer and processed as described in (Herbert et al., 2006). In brief, lysates were incubated with a telomerase substrate and incubated at 30˚C for telomerase to add telomere repeats. The reactions were then PCR amplified. Telomere repeats were resolved on a 4-20% TBE polyacrylamide gel and visualized by staining with SYBR Green nucleic acid gel stain. Relative telomerase activity was quantified using ImageJ focusing on the first six amplicons averaged across the dilutions.

Measurement of Telomere Lengths by TRF and TeSLA

Telomere lengths were measured as described in (Lai et al., 2016, 2017). DNA was isolated from cells using a Gentra Puregene kit (Qiagen). DNA was quantified by fluorometry using QuBit 2.0 (Invitrogen). For TRF analysis in brief, 500 ng of DNA was digested with CviAII overnight followed by digestion with a mixture of BfaI, MseI, and NdeI overnight. For TeSLA in brief, 50 ng of DNA was ligated to telorette adapters, then digested with CviAII, then digested with a combination of BfaI, MseI and NdeI, dephosphorylated, and TeSLA adapters (AT/TA Adapters) were ligated on. These TeSLA libraries were PCR amplified using Lucigen's FailSafe polymerase kit with Pre-Mix H.

Southern blotting was carried out using previously established protocols with some modification (Kimura et al., 2010; Lai et al., 2017). TRFs and TeSLA PCR reactions were separated on a 0.7% agarose gel at 0.833 V/cm for 24 hours. The gel was depurinated and denatured and then transferred to a Hybond XL membrane (Cytiva) by capillary transfer using denaturation buffer. The Hybond membrane was hybridized using a DIG-labeled telomere probe overnight. The blot was then washed

and exposed using CDP-Star on an LAS-4000 Image Quant imager (Cytiva). TRFs were analyzed using ImageQuant while TeSLAs were analyzed using the MatLab software developed previously (Lai et al., 2017).

Measurement of Telomere Lengths by qPCR

Average telomere length was measured by qPCR as described in (Cawthon, 2002; Joglekar et al., 2020) with some modifications. In brief, isolated genomic DNA was quantified by QuBit fluorometry (Invitrogen) and diluted to within the range of a standard curve constructed from a mixture of all samples analyzed. Triplicate qPCR reactions of the Telomeric (T) product and the Single copy gene (S) (*HBB*) were amplified using a Roche LightCycler 480 II (Roche) using the following programs: T PCR Program 95˚C for 10 minutes, 40 cycles of 95˚C for 15 seconds, 56˚C for 1 minute; S PCR Program 95˚C for 10 minutes, 40 cycles of 95˚C for 15 seconds, 58˚C for 1 minute. Cq values were computed using the second derivative method, and T/S ratios were calculated using the $2^{-\Delta\Delta Ct}$ method.

RNA-Sequencing and Data Analysis

SPC+ sorted cells from the indicated times during, counted and harvested in TRIzol and stored at -80 °C until further processing. The RNA was isolated using a Direct-Zol kit (Zymo Research). RNA concentration was obtained by QuBit fluorometry (Invitrogen) and the integrity was checked by tape station analysis (Agilent Technologies). All samples had RINs >8, and the libraries were prepared by poly-A selection and sequenced by GeneWiz, LLC.

RNA sequencing libraries were prepared using the NEBNext Ultra RNA Library Prep Kit for Illumina following manufacturer's instructions (NEB). Briefly, mRNAs were first enriched with Oligo(dT) beads. Enriched mRNAs were fragmented for 15 minutes at 94 °C. First strand and second strand cDNAs were subsequently synthesized. cDNA fragments were end repaired and adenylated at 3'ends, and universal adapters were ligated to cDNA fragments, followed by index addition and library enrichment

by limited-cycle PCR. The sequencing libraries were validated on the Agilent TapeStation (Agilent Technologies), and quantified using a Qubit 2.0 Fluorometer (Invitrogen) as well as by quantitative PCR (KAPA Biosystems).

The sequencing libraries were pooled and clustered on one lane of a flowcell. After clustering, the flowcell was loaded on the Illumina HiSeq instrument (4000 or equivalent) according to manufacturer's instructions. The samples were sequenced using a 2x150bp paired end configuration. Image analysis and base calling were conducted by the HiSeq control software . Raw sequence data (.bcl files) generated from Illumina HiSeq was converted into fastq files and de-multiplexed using Illumina's bcl2fastq 2.17 software. One mismatch was allowed for index sequence identification.

Fastq files were checked for quality using FastQC. Raw sequence files (fastq) for 22 samples were mapped using salmon (https://combine-lab.github.io/salmon/)(Patro et al., 2017) against the human transcripts described in Gencode (version v33, built on the human genome GRCm38, https://www.gencodegenes.org), with a 70.5% average mapping rate yielding 30.4M average total input reads per sample. Transcript counts were summarized to the gene level using tximport (https://bioconductor.org/packages/release/bioc/html/tximport.html), and normalized and tested for differential expression using DESeq2 (https://bioconductor.org/packages/release/bioc/html/DESeq2.html). Subsets of time-matched samples were used to compute pair-wise contrast statistics for mutant *vs.* wt at each time.

Gene set enrichment analysis (GSEA) (Subramanian et al., 2005) was carried out in R (v4.0.2) (Team, R Core, 2020) using RStudio (v1.3.1056) (RStudio Team, 2020), the tidyverse (v1.3.0) (Wickham et al., 2019), and the readxl package (v1.3.1) (Hadley Wickham, 2019). GSEA was run for contrasts of interest in pre-ranked mode using the DESeq2 statistic as the ranking metric(Love et al., 2014). Annotated molecular signatures from the Hallmark Collection (H), Curated Collection (C2), and

Regulatory Target Molecular Collection (C3) maintained by the Molecular Signatures Database were accessed in RStudio using the msigdbr package (v7.1.1) (Dolgalev, 2020; Liberzon et al., 2011, 2015). The clusterProfiler package (v3.17.1) was used to perform GSEA on the unfiltered, sorted gene lists (Yu et al., 2012). GSEA results were viewed using the DT package (v0.15) (Yihui Xie, 2020). GSEA plots were generated using the enrichplot package (v1.9.1) (Yu, 2020).

Genes that differed in expression >2 fold and were associated with an adjusted p-value < 0.05 from the D70 time point were also analyzed through the use of Ingenuity Pathway Analysis (Ingenuity® Systems, www.ingenuity.com) (Krämer et al., 2014) through the University of Pennsylvania Molecular Profiling Facility.

Statistical Methods

Statistical methods are outlined in each of the figure legends. Each replicate "n" represents an entirely separate differentiation from the pluripotent stem cell stage. Quantitative data is represented as the mean with error bars representing the standard error of the mean. Student's t-tests (unpaired and two-tailed) were used for determining statistical significance for all comparisons unless otherwise noted.

Acknowledgments

We would like to thank Drs. Eric Witze, Peter Klein, Timothy Olson, Andrew Vaughan, Leo Cardenas, Aravind Sivakumar for fruitful discussions. We would like to thank Dr. Dong Hun Woo, Carla Hoge, John McCormick and Dr. Rachel Truitt for help culturing iPS cells, and Dr. Darrell Kotton for providing the BU3 NGST line. This work was supported by NIH grants R01HL148821 (F.B.J. and C.J.L), R21AG054209 (F.B.J. and C.J.L.) and 5T32AG000255 (R.J.F.), and a grant from Team Telomere and the Penn Orphan Disease Center. This work was also supported in part by the National Institute of Diabetes and Digestive and Kidney Diseases (NIDDK) Center for Molecular Studies in Digestive and Liver Diseases (P30DK050306) and its Molecular Profiling and Imaging core facilities, by the University of Pennsylvania induced Pluripotent Stem Cell Core and the Penn Genomic Analysis Core,

by the Flow Cytometry Core Laboratory and the Human Pluripotent Stem Cell Core at the Children's Hospital of Philadelphia Research Institute.

Author Contributions

Conceptualization, R.J.F., C.J.L., and F.B.J.; Methodology, R.J.F., Z.J.G.G., K.S., W.Y., E.E.M., D.C.L., J.W.T., A.B., M.P.M., and F.B.J.; Investigation, R.J.F., Z.J.G.G., G.T.S., J.V.P., Q.C., S.R., R.B., K.N.E., C.J.L., and F.B.J.; Writing – Original Draft, R.J.F. and F.B.J.; Writing – Review & Editing, R.J.F., D.C.L., C.J.L. and F.B.J.; Funding Acquisition, C.J.L. and F.B.J.; Resources, W.Y., E.E.M., D.B.F., C.J.L. and F.B.J.; Supervision, F.B.J. and C.J.L.

Declaration of Interests

No competing interests to declare.

Figures

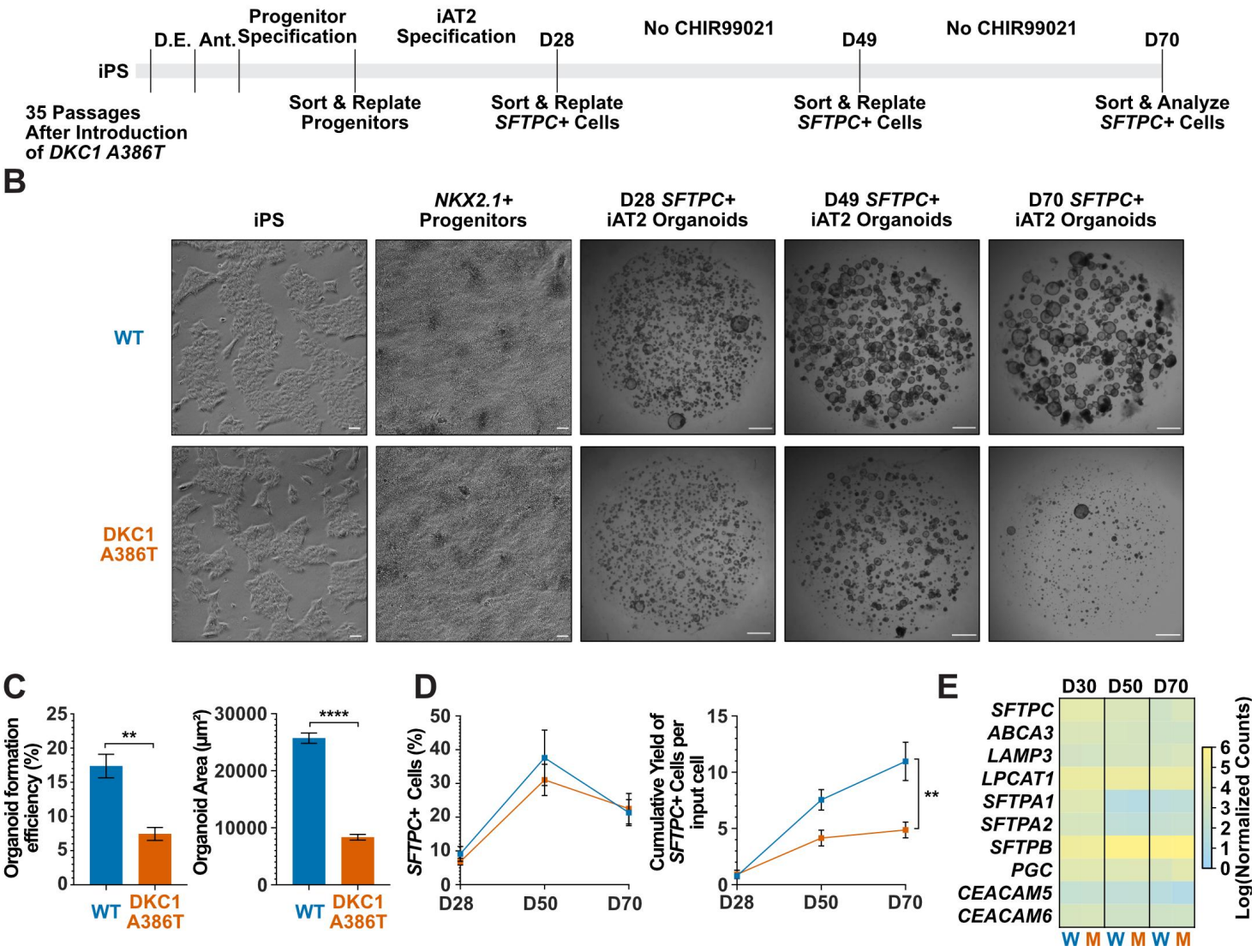

Figure 1. DC iAT2s fail to form alveolospheres with successive passaging

(A) Differentiation protocol used to probe the effects of the *DKC1 A386T* mutation on iAT2 cells. (D.E. - Definitive Endoderm Specification; Ant. - Anteriorization)

(B) Representative images of differentiating WT and *DKC1 A386T* mutant bearing iAT2 alveolospheres. (scale bars, 100 μm as indicated for iPS and *NKX2.1*+ progenitors; 1 mm for all alveolosphere images)

(C) Quantifications of alveolosphere area and formation efficiency on D70. (n = 4; ** $p < 0.01$, **** $p < 0.0001$, Student's t-test)

(D) Quantification of the percentage *SFTPC*+ cells and the number of *SFTPC*+ cells produced with passage of the iAT2 cells shows *DKC1 A386T* iAT2 alveolospheres accumulate fewer *SFTPC*+ cells. (n = 4; ** $p < 0.01$, Student's t-test)

(E) RNAseq of sorted *SFTPC*+ iAT2 cells at different passages show AT2 cell genes are not grossly affected by the *DKC1 A386T* mutation. (n = 4). *W* = wild type, *M* = mutant.

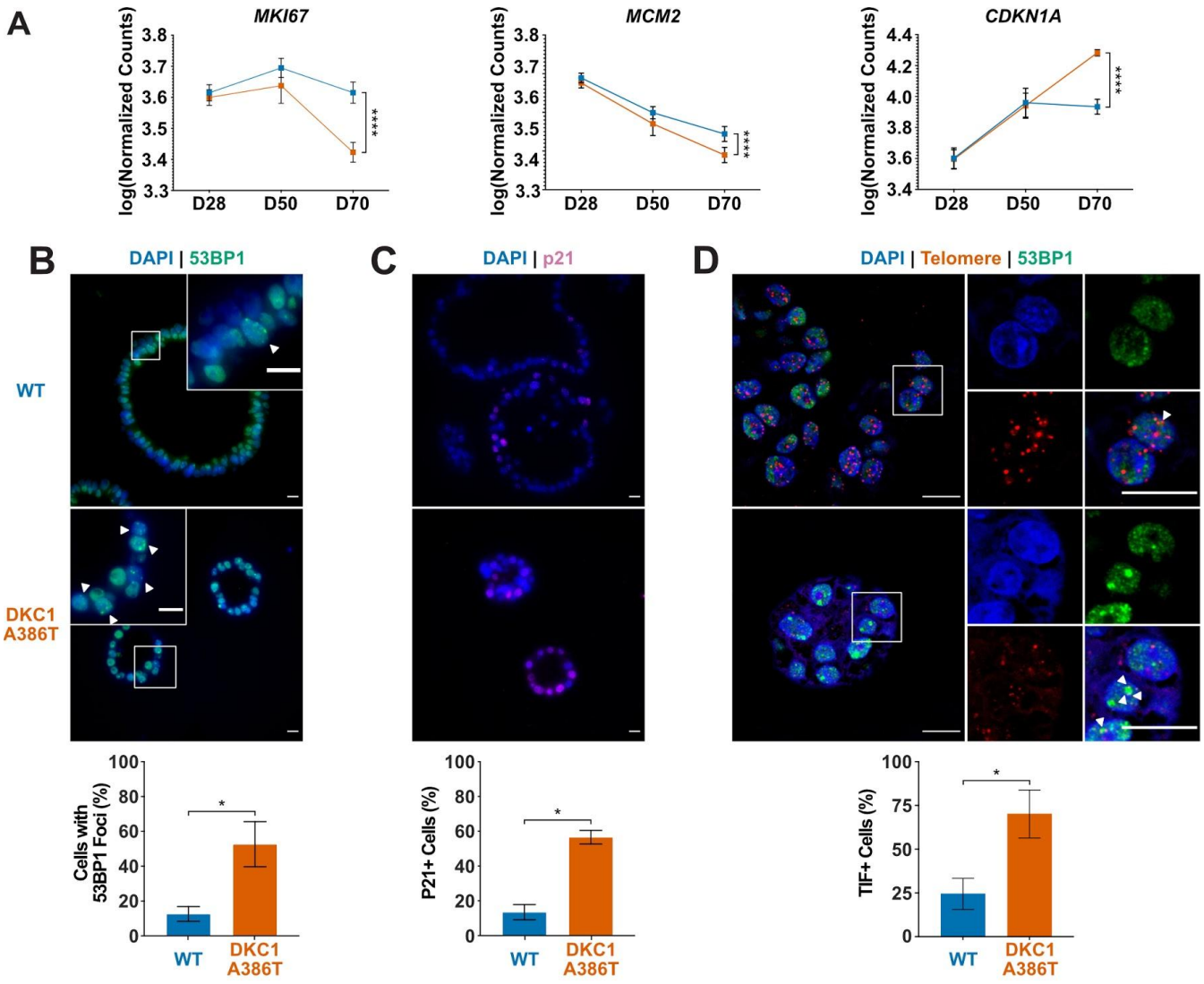

Figure 2. DC iAT2s at D70 show hallmarks of senescence

(A) Gene expression profiling of iAT2 cells at D28 and D50 show no difference between WT and *DKC1 A386T* in expression of markers of proliferation and a cell cycle inhibitor, while at D70 cells, there is a significant decrease in *MCM2* and *MKI67* as well as a significant increase in *CDKN1A* (p21). (n = 4, **** $p < 0.0001$, DEseq2 pairwise contrast statistics)

(B) At D70, *DKC1 A386T* mutant iAT2 cells have a higher fraction of cells with 53BP1 foci. (n = 4, * $p < 0.05$, Student's t-Test; scale bars, 10 μm; Insets highlight cells with 53BP1 foci as noted by the white arrowheads)

(C) At D70, *DKC1 A386T* mutant iAT2s have a higher fraction of cells positive for p21. (n = 4, * $p < 0.05$, Student's t-Test; scale bars, 10 μm)

(D) At D70, *DKC1 A386T* mutant iAT2s have a higher fraction of cells with TIFs. (n = 4, * $p < 0.05$, Student's t-Test; scale bars, 10 μm; Insets highlight cells with TIFs, each one noted by a white arrowhead)

(E) Representative TeSLA of *DKC1 A386T* iAT2 alveolospheres shows telomeres shorten with passage.

(F) Quantification of *DKC1 A386T* iAT2 cell telomere lengths shows a preponderance of short telomeres appears as the iAT2 cells approach D70, red colored data points highlight telomeres under the 1.6kb threshold. (n = 2, "Shortest 20%" reports the 20th percentile of telomere length, in Kb)

A

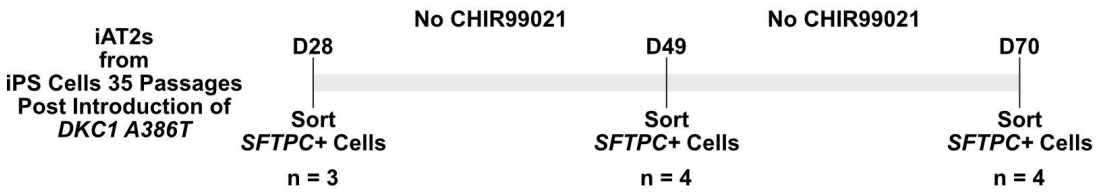

B

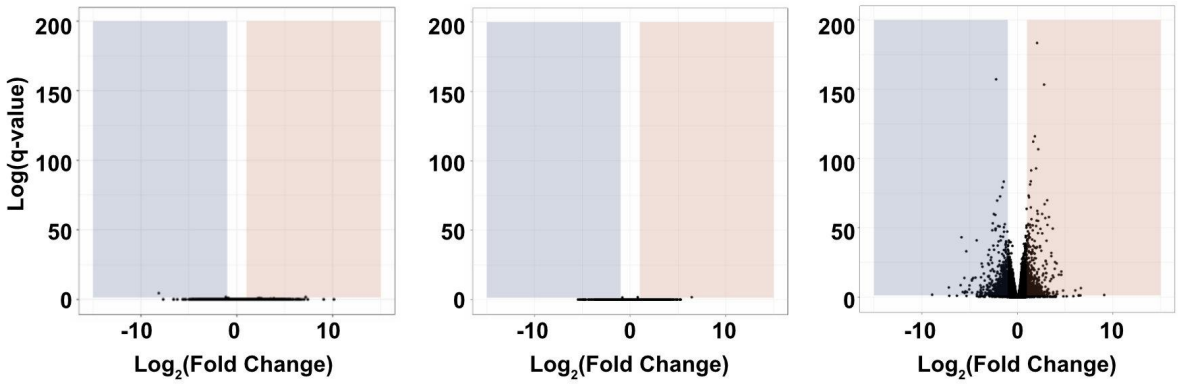

C

Gene Set	Day 70 NES	Day 70 p-adj
REACTOME_WNT5A_DEPENDENT_INTERNALIZATION_OF_FZD2_FZD5_AND_ROR2	1.69070396	0.02104417
REACTOME_BETA_CATENIN_INDEPENDENT_WNT_SIGNALING	1.6795837	0.00099486
REACTOME_WNT5A_DEPENDENT_INTERNALIZATION_OF_FZD4	1.65435977	0.03365137
REACTOME_PCP_CE_PATHWAY	2.00331167	3.7613E-06

D

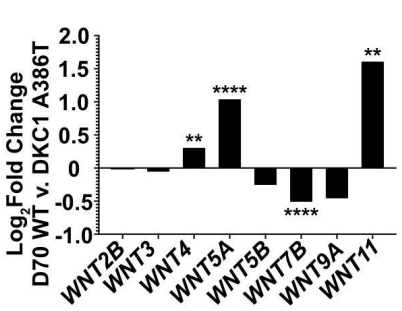

E

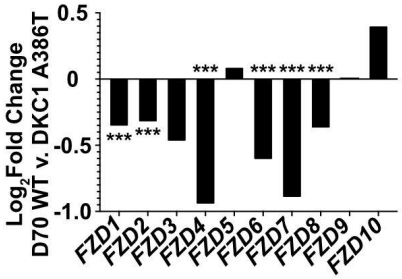

H

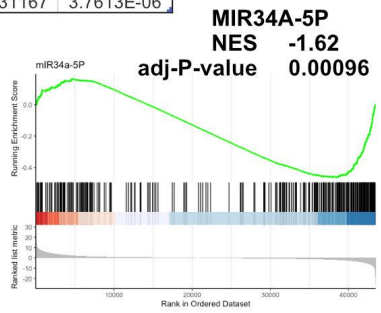

F

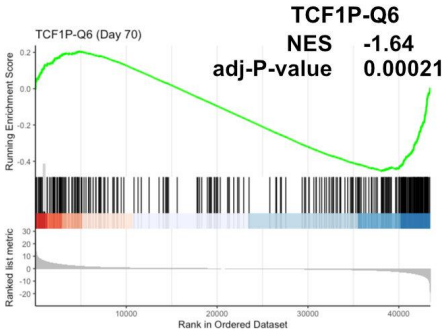

G

Master Regulator	Predicted Activation	Activation z-score	Overlap p-value	Network bias-corrected p-value
Lithium Chloride	Inhibited	-2.721	6.74E-14	0.02
TCF7	Inhibited	-2.394	1.22E-08	0.03
SFRP4	Activated	2.1	1.15E-11	1.40E-03
FRZB	Activated	2.331	8.14E-14	1.14E-02
SFRP1	Activated	2.744	2.94E-11	4.32E-02

I

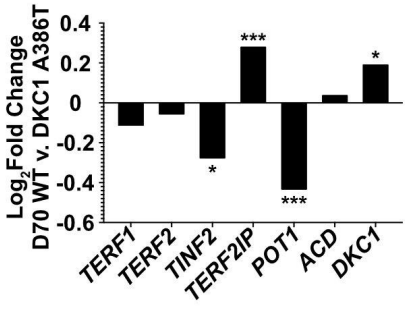

Figure 3. RNA-seq of passaged iAT2 cells reveals a time dependent change in Wnt signaling

(A) A schematic to show how cells were prepared for RNA-seq.

(B) Volcano plots at D28, D50, and D70 show how the number of differentially expressed genes increases at D70.

(C) GSEA Analysis at D70 comparing *DKC1 A386T* iAT2 cells reveals an upregulation of non-canonical Wnt Signaling and the PCP (Planar Cell Polarity) pathway.

(D) RNA-seq analysis shows upregulation of *WNT5A* and *WNT11*, non-canonical WNTs associated with pulmonary fibrosis. (* $p < 0.05$, ** $p < 0.01$, *** $p < 0.001$, **** $p < 0.0001$, DEseq2 pairwise contrast statistics)

(E) RNA-seq analysis shows broad downregulation of many *FZD* receptors. (* $p < 0.05$, ** $p < 0.01$, *** $p < 0.001$, **** $p < 0.0001$, DEseq2 pairwise contrast statistics)

(F) GSEA Analysis at D70 comparing *DKC1 A386T* iAT2 cells reveals an downregulation of genes with *TCF7* bindings sites in their promoters.

(G) Ingenuity Pathway Analysis reveals master regulators at D70 including downregulation of Lithium chloride, *TCF7*, and upregulation of multiple Wnt inhibitors.

(H) GSEA Analysis at D70 comparing *DKC1 A386T* iAT2 cells reveals a downregulation of genes with *miR34A* binding sites.

(I) *TINF2* and *POT1* are downregulated in *DKC1 A386T* iAT2 cells at D70. (* $p < 0.05$, ** $p < 0.01$, *** $p < 0.001$, DEseq2 pairwise contrast statistics)

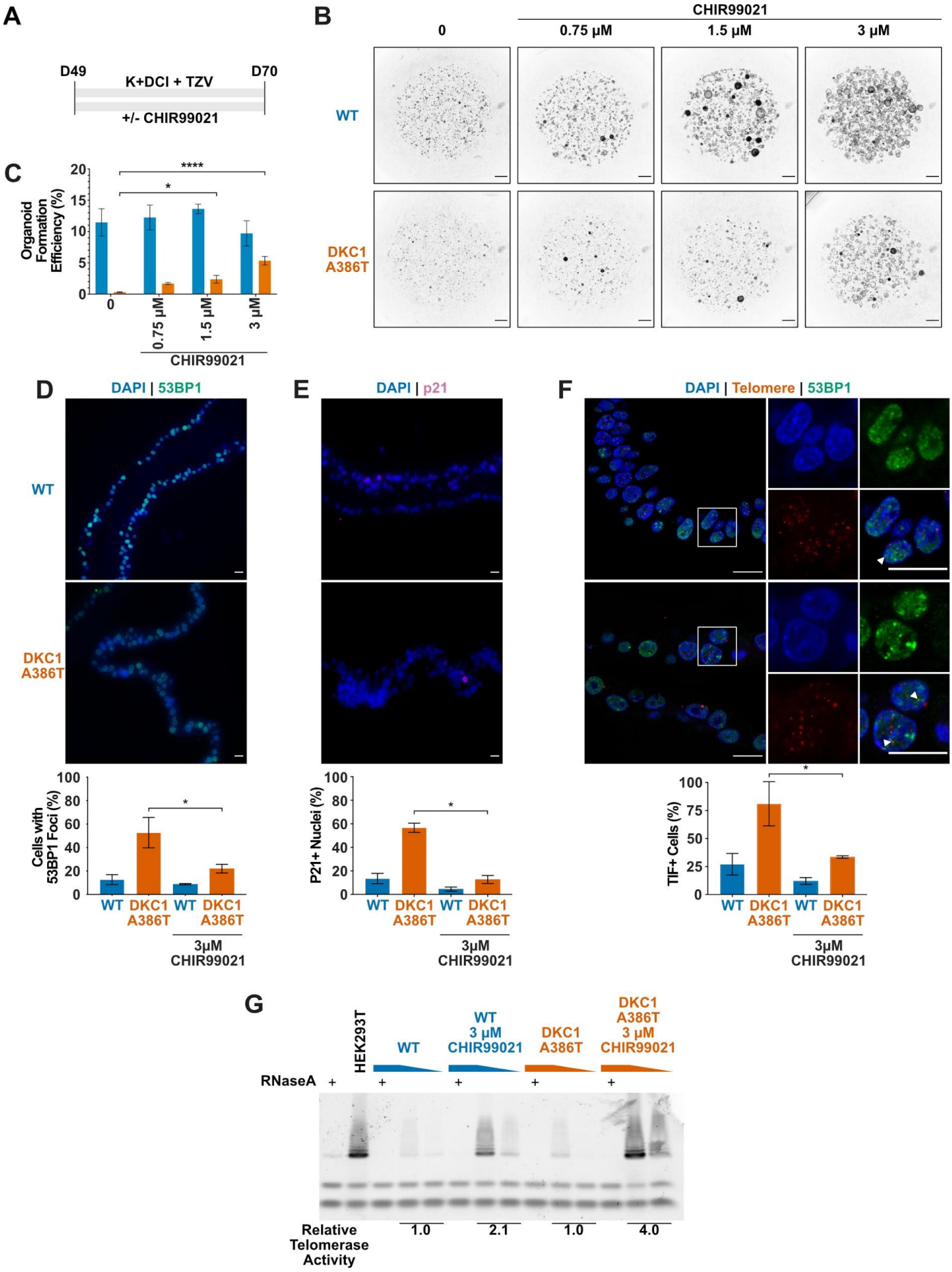

Figure 4. CHIR99021 rescues growth and telomere defects in DC iAT2 cell alveolospheres

(A) Differentiation protocol used to test how CHIR99021 affects growth of DC iAT2s.

(B) Representative images of differentiating WT and *DKC1 A386T* mutant bearing cells with increasing amounts of CHIR99021. (scale bars, 1 mm for all alveolosphere images)

(C) Quantifications of alveolosphere formation efficiency after treatment with differing concentrations of CHIR99021. (n = 4, * $p < 0.05$, **** $p < 0.0001$, Student's t-test)

(D) When D70 alveolospheres are cultured with 3 μM CHIR99021, *DKC1 A386T* mutant iAT2 cells have a lower fraction of cells with 53BP1 foci. Note, data for no CHIR99021 bars are from Figure 2. (n = 3, * $p < 0.05$, Student's t-test; scale bars, 10 μm)

(E) When D70 alveolospheres are cultured with 3 μM CHIR99021, *DKC1 A386T* mutant iAT2 cells have a lower fraction of p21 positive cells. Note, data for no CHIR99021 bars are from Figure 2. (n = 3, * $p < 0.05$, Student's t-test; scale bars, 10 μm)

(F) When D70 alveolospheres are cultured with 3 μM CHIR99021, *DKC1 A386T* mutant iAT2 cells have a lower fraction of TIF positive cells. Note, data for no CHIR99021 bars are from Figure 2. (n = 3, * $p < 0.05$, Student's t-test; scale bars, 10 μm; Insets highlight cells with TIFs, each one noted by the white arrowheads)

(G) Telomeric repeat amplification protocol (TRAP) assay for telomerase activity in iAT2 cells using 5-fold extract dilutions. (n = 2)

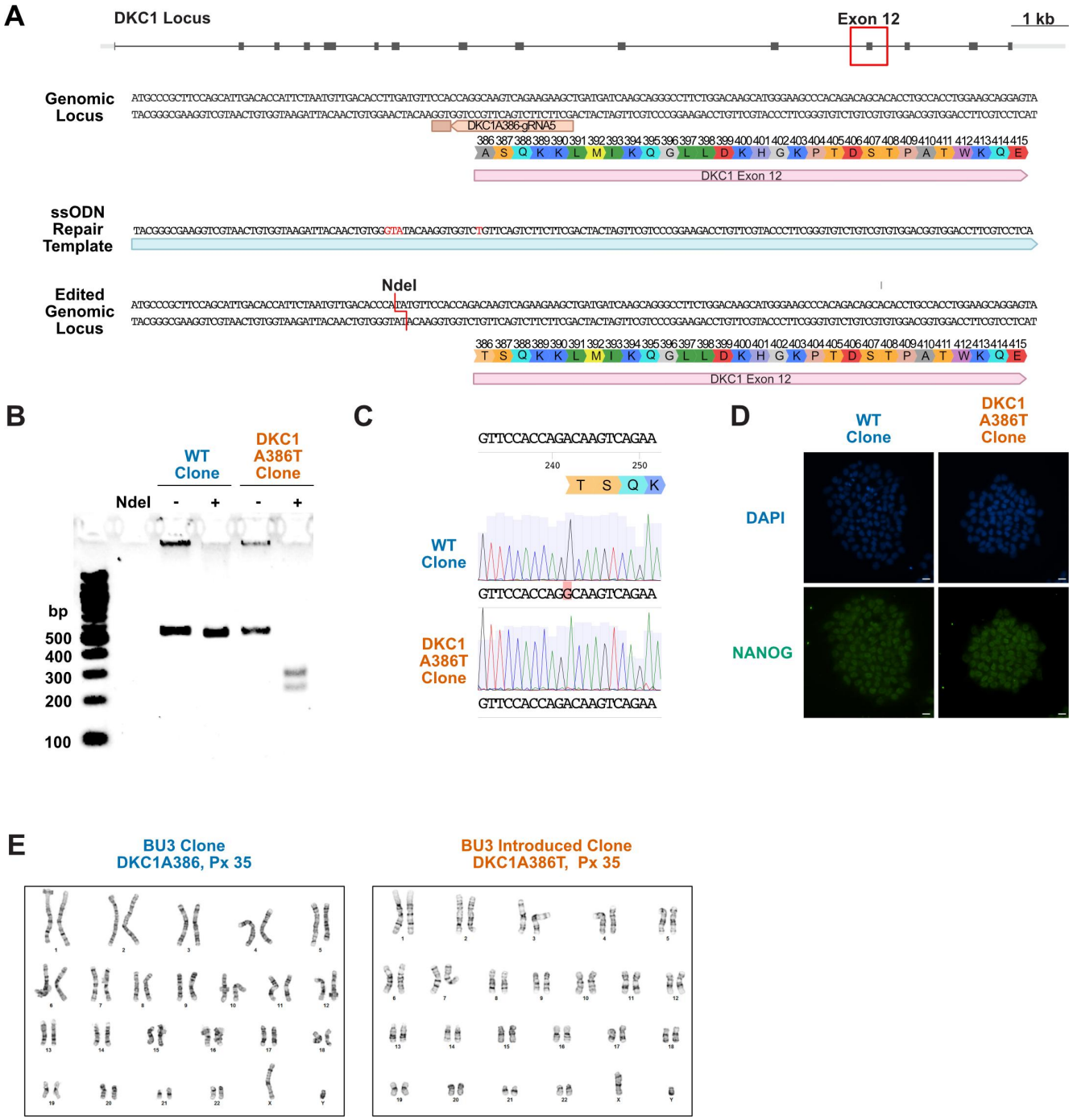

Figure S1. Introduction of the *DKC1 A386T* mutation into the BU3 *NKX2.1::GFP, SFTPC::TdTomato* iPS Cell Line

(A) CRISPR based editing strategy for introducing the *DKC1 A386T* mutation into the BU3 *NKX2.1::GFP, SFTPC:: TdTomato* iPS cell line.

(B) Genotyping by RFLP of *DKC1 A386T* clonal cell lines and their WT counterparts that also were exposed to the CRISPR reagents using the introduced NdeI site.

(C) Sanger sequence verification of the introduction of the mutation yielding 1156G>A. Note the WT sequence is marked in red.

(D) Paired iPS cell clones maintain high expression of NANOG, a marker of pluripotency. (scale bars, 100 μm)

(E) Paired iPS cell clones show normal karyotypes after the introduction of the *DKC1 A386T* mutation.

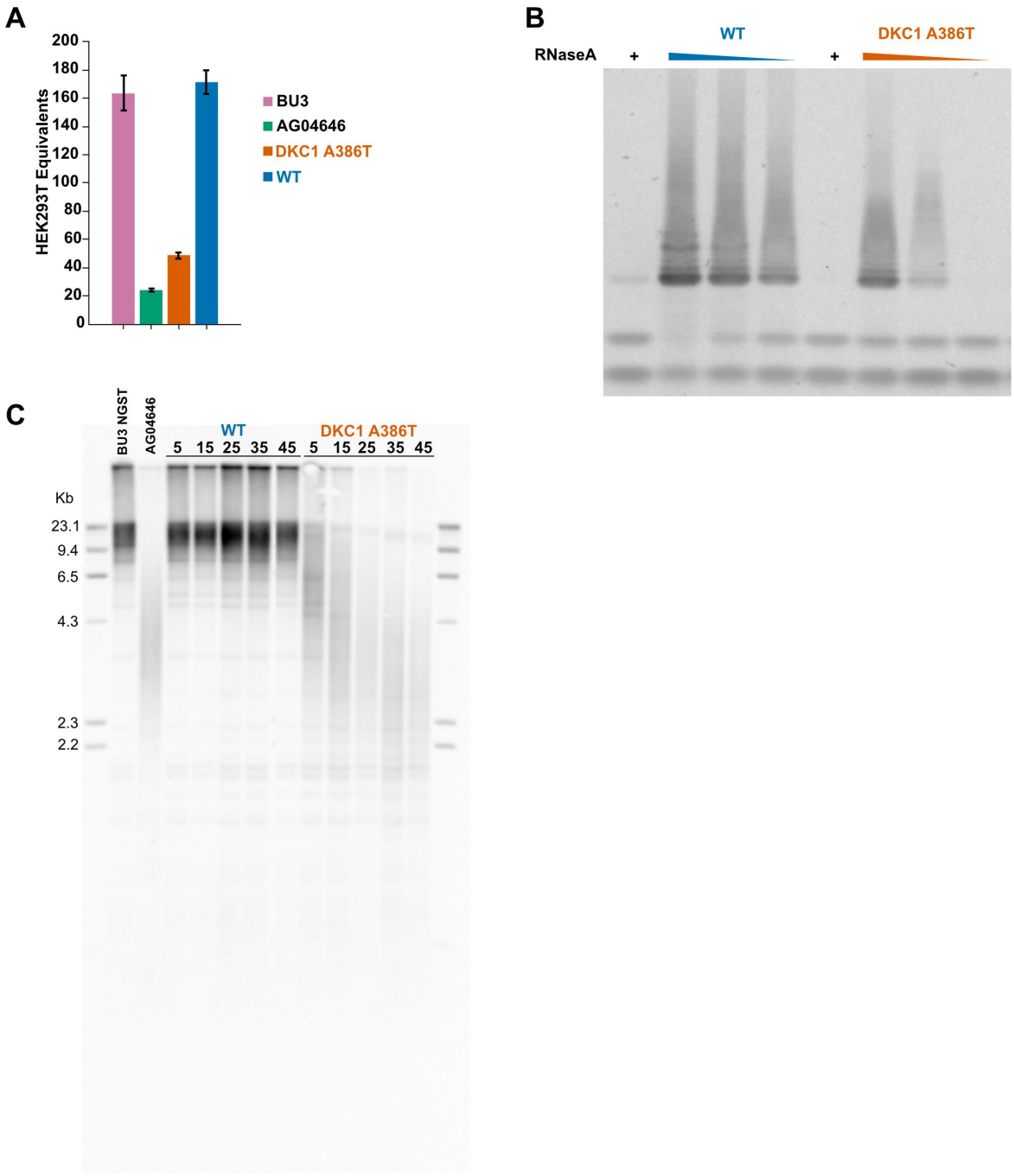

Figure S2. *DKC1 A386T* iPS cells show decreased telomerase activity and telomeres shorten with passage

(A) Quantitative telomeric repeat amplification protocol (qTRAP) assay for telomerase activity in iPS cells shows a reduction in relative telomerase activity in *DKC1 A386T* introduced lines. (n = 3)

(B) Telomeric repeat amplification protocol (TRAP) assay for telomerase activity in iPS cells using a 5 fold dilution series of the cellular extracts show a reduction in relative telomerase activity in DKC1 A386T introduced lines.

(C) Terminal restriction fragment (TRF) telomere length analyses in the WT and *DKC1 A386T* paired iPS cells compared to the parental iPS Line (BU3 NGST) and the patient derived iPS line (AG04646). Above each lane is the number of passages from the introduction of the mutation.

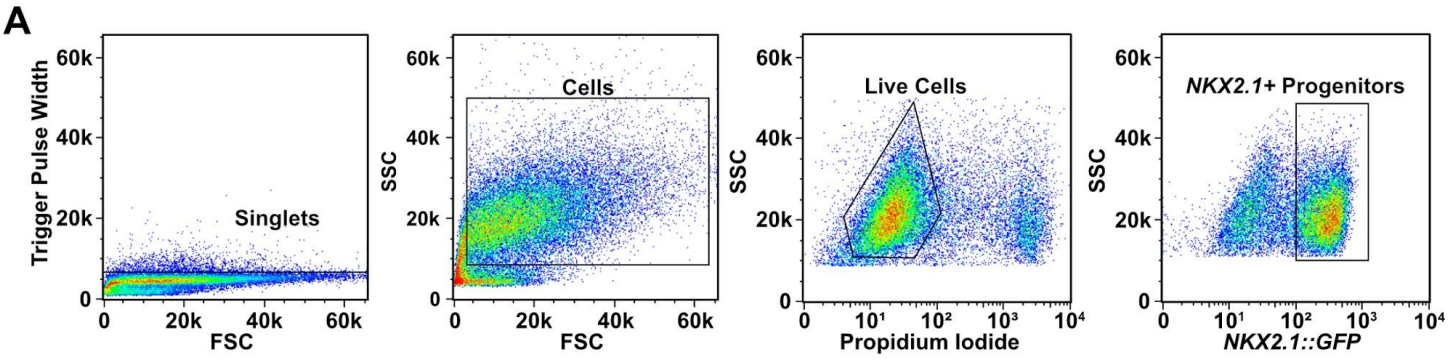

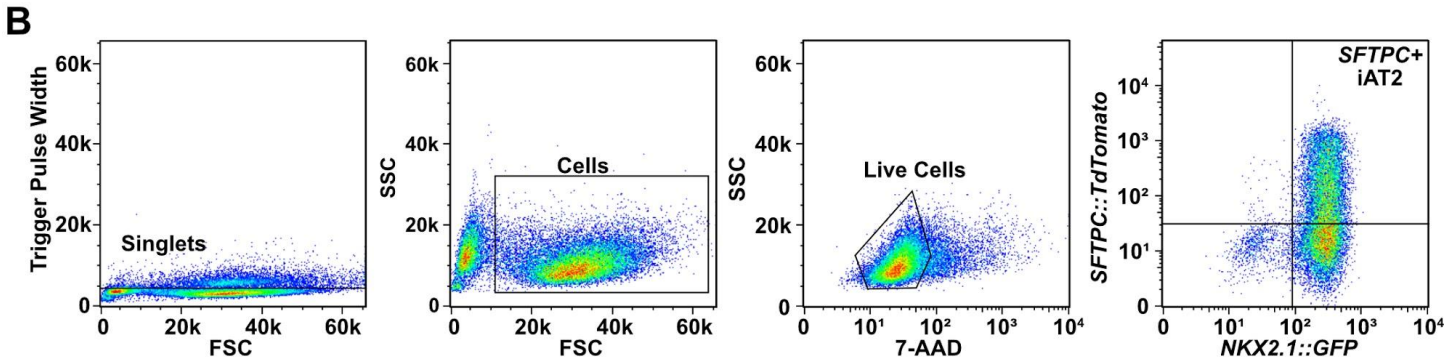

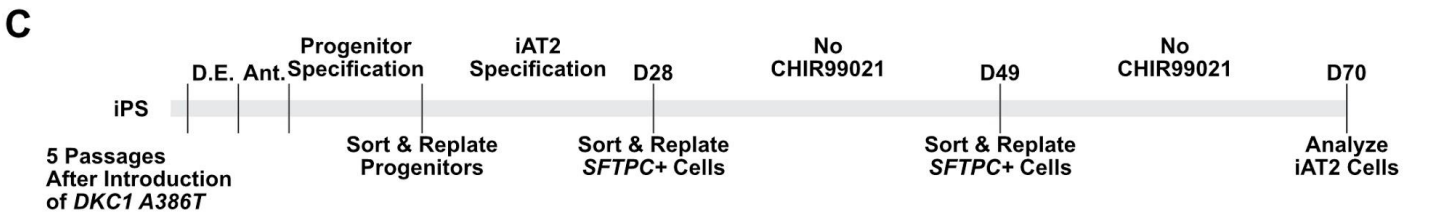

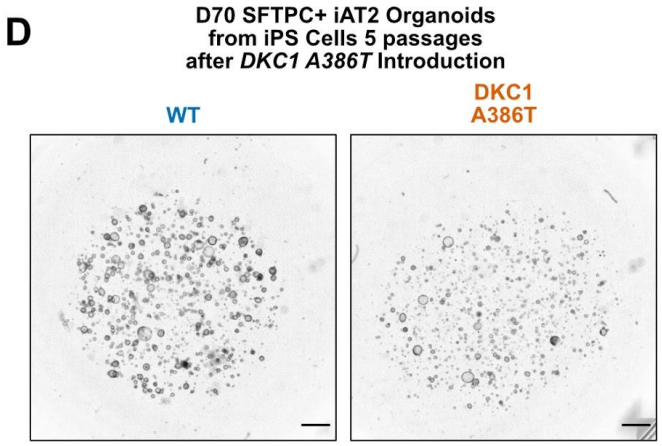

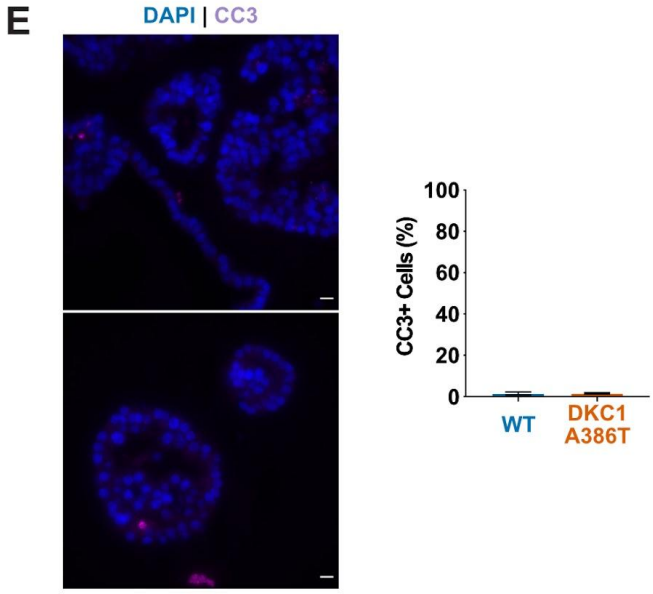

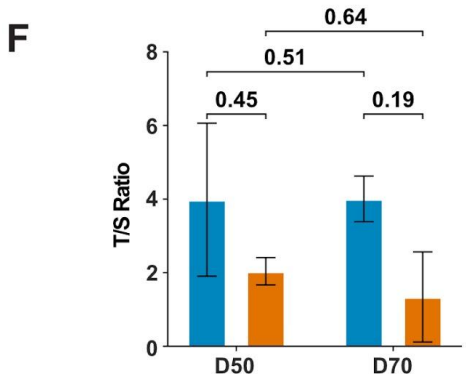

Figure S3. Representative sorting strategies and differentiation of early passage iPS cells yields no growth defect

(A) Representative sorting strategy for *NKX2.1*+ progenitors.

(B) Representative sorting strategy for *SFTPC*+ cells from iAT2 alveolospheres.

(C) Differentiation protocol used to probe the effects of the *DKC1 A386T* mutation on iAT2 cells. (D.E. - Definitive Endoderm Specification; Ant. - Anteriorization)

(D) Representative images of differentiating WT and *DKC1 A386T* mutant bearing iAT2 alveolospheres derived from iPS cells that have undergone 5 passages after introduction of the mutation. (scale bars, 1 mm)

(E) Representative images and quantification of CC3 staining at D70 shows no significant difference between WT and *DKC1 A386T* mutant iAT2s. (n = 4, no difference, p = 0.96, Student's t-test)

(F) Average telomere length as measured by telomere qPCR of WT and DC iAT2 cells with passage (n = 2, p-values listed on the figure)

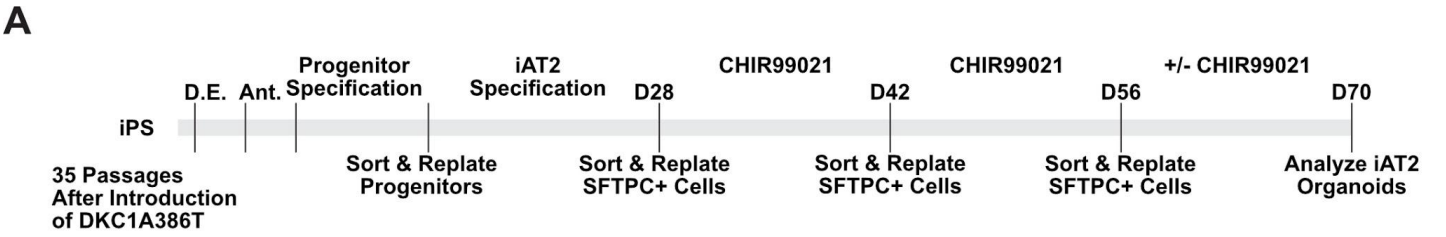

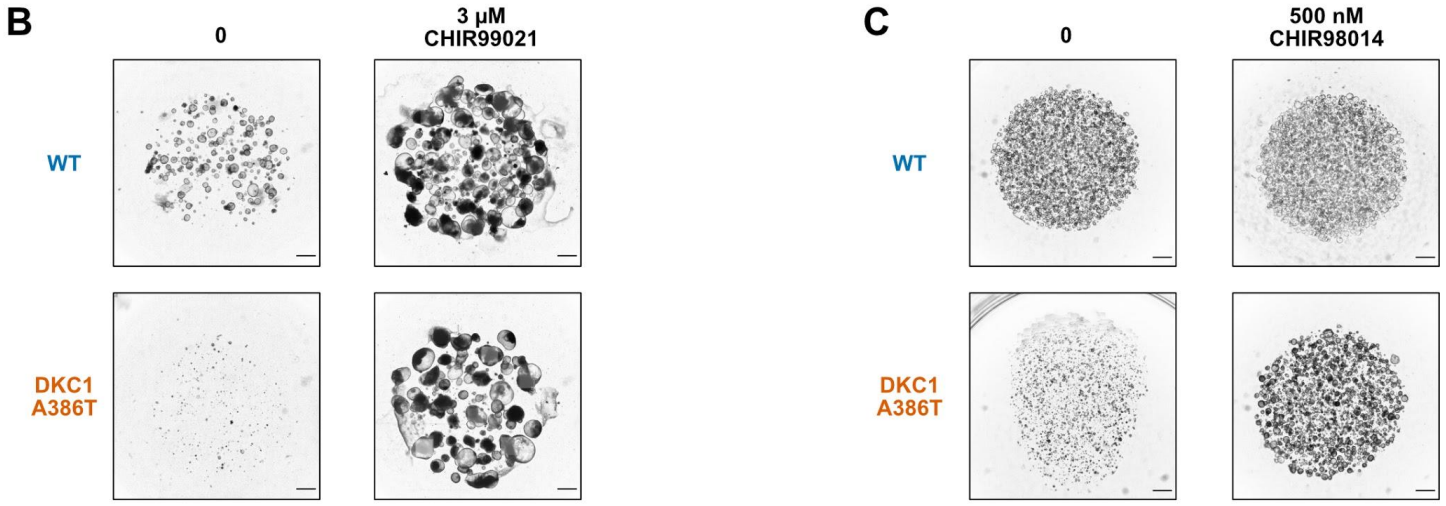

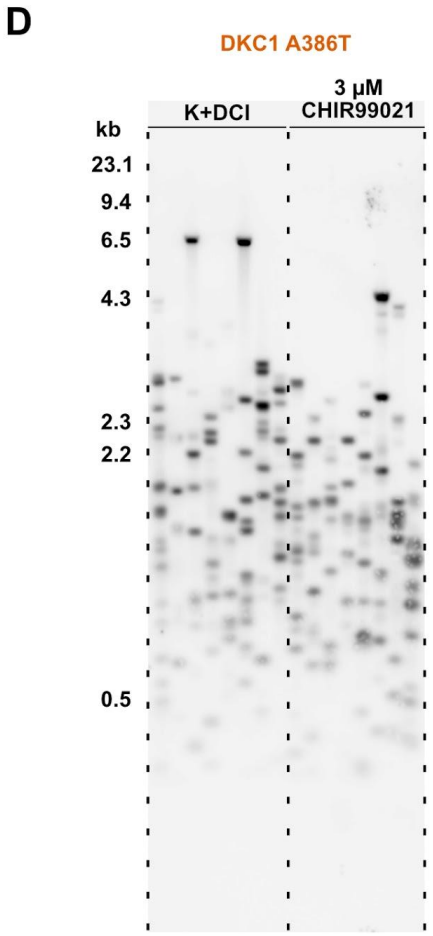

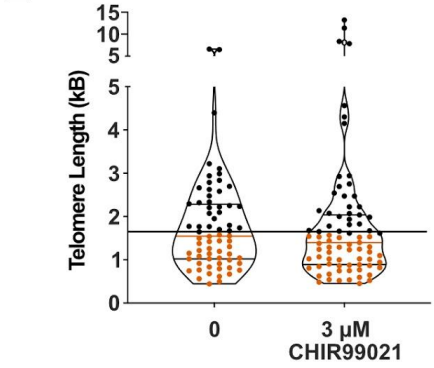

	0	3 μM CHIR99021
Average	1.79	2.2
Below 1.6 Kb	53%	59%
Shortest 20%	0.92	0.86

875

Figure S4. Pre-treatment with CHIR99021 does not prevent the growth defect or lengthen telomeres in DC iAT2 cells

(A) Differentiation protocol used to test how pre-treatment culture with CHIR99021 affects growth of DC iAT2s.

(B) Representative images of iAT2 alveolospheres at D70 with and without CHIR99021 shows that pre-treatment does not prevent the defect when CHIR99021 is removed. (scale bars, 1 mm)

(C) Rescue of DC iAT2 alveolosphere growth with CHIR98014. These alveolospheres grew from cells plated at 400 cells/μL. (scale bars, 1 mm)

(D) TeSLA of *DKC1 A386T* iAT2 alveolospheres treated with 3 μM CHIR99021 shows no difference in telomere length.

(E) Quantification of TeSLA blot of *DKC1 A386T* iAT2 alveolospheres shows no difference in average telomere length or in fraction of shortest telomeres. (n = 1, “Shortest 20%” reports the 20th percentile of telomere length, in Kb)

Tables

Supplementary Table 1. Differentially expressed pathways from D70 DC iAT2 cells that are similar to changes seen in IPF

These tables display selected results from GSEA and IPA analyses that highlight pathways found to be differentially regulated in mutant iAT2 cells at D70 when compared to wildtype cells. The first table displays GSEA results along with the pathway name, normalized enrichment score (NES) and adjusted p-value (D70 p-adj). The second table displays IPA results from the Canonical Pathways analysis. These are gene sets that are differentially regulated in mutant iAT2 cells at D70 when compared to wildtype cells. The p-value reports the significance of enrichment of the molecules in that gene set, and the activation score reports how concordant the gene expression changes are with what is predicted from the literature embedded in IPA (a negative z-score argues that the gene set is down regulated in the mutant iAT2 cells, whereas a positive z-score argues that the gene set is upregulated in mutant iAT2 cells; the lack of a z-score is indicative there was insufficient evidence to provide a z-score.) The “molecules” column lists the genes that were in that gene set that were also found in our differentially expressed gene list when comparing mutant iAT2 cells to wildtype cells.

Supplementary Table 2. GSEA results comparing D70 DC to WT iAT2 cells

These tables provide the unedited output of the GSEA analysis using the C2 curated gene sets, H hallmark gene sets, and C3 regulatory target gene sets when comparing D70 mutant to wild type iAT2 cells. The table reports the name of the gene set (ID), the size of the gene set (setSize), the raw enrichment score (enrichmentScore), the normalized enrichment score (NES), along with the p-value, the adjusted p-value (p.adjust) and false discovery rate q-value (q-values). The “coreenrichment” column displays the genes in the gene set.

Supplementary Table 3. IPA results comparing D70 DC to WT iAT2 cells

These tables provide the unedited output of the IPA analysis. The summary tab lists metadata associated with the analysis. The “Analysis Ready Molecules” lists the differentially expressed genes that differed in expression >2 fold and were associated with an adjusted p-value < 0.05 from D70 mutant iAT2 cells (DEG list). The “Canonical Pathways tab” lists pathways curated from the literature and the p-value for enrichment using the DEG list used in the IPA analysis. The “Upsteam Regulators” tab lists the transcription factors, cytokines and other genetic regulators whose target genes are in the DEG list. “Causal Networks” seeks to build a regulatory network based off of the “Upstream Regulators” to identify master regulators of the DEG list. For more information on interpreting ingenuity analysis results see (Krämer et al., 2014).

925

926 **Key Resource Table**